ISPRS Journal of Photogrammetry and Remote Sensing 194 (2022) 39–57

Contents lists available at ScienceDirect

ISPRS Journal of Photogrammetry and Remote Sensing

journal homepage: www.elsevier.com/locate/isprsjprs

Mapping water clarity in North American lakes and reservoirs using Landsat images on the GEE platform with the RGRB model

Qiang Wang [a,1], Kaishan Song [a,1], Xiangming Xiao [b], Pierre-Andre Jacinthe [c], Zhidan Wen [a], Fangrui Zhao [a], Hui Tao [a,d], Sijia Li [a], Yingxin Shang [a], Yu Wang [e], Ge Liu [a,*]

[a] Northeast Institute of Geography and Agroecology, CAS, Changchun 130102, China
[b] Department of Microbiology and Plant Biology, OU, Norman, OK 73019 USA
[c] Department of Earth Sciences, IUPUI, INpolis, IN 46202, USA
[d] University of Chinese Academy of Sciences, Beijing 100049, China
[e] Center for Satellite Application on Ecology and Environment, Ministry of Ecology and Environment, Beijing 100006, China

A R T I C L E I N F O

Keywords:
Water clarity
Landsat imagery
Google Earth Engine
Top-of-atmosphere reflectance

A B S T R A C T

Lakes and reservoirs provide important ecosystem services that support human welfare and socio-economic activities. However, in many world regions, the ecological integrity of lakes and reservoirs is threatened by human perturbations and climate change. The Secchi disk depth (SDD) is a widely-used proxy representing the trophic status of lakes and reservoirs and can be retrieved from remote sensing data. Despite their potential for large-scale (regional, global) and long-term lake and reservoir water clarity assessment, the transferability of remote sensing-based models has been a major limitation. In this study, we assembled in situ SDD in lakes and reservoirs across North America (NA) from five different sources. We identified a subset of 3235 samples collected within ±7 days of a Landsat satellite overpass. Relationships between various spectral index models calculated from Landsat top-of-atmosphere reflectance and in situ SDD were analyzed. A model based on Landsat blue/green plus blue/red ratios (denoted as RGRB) was selected to retrieve the SDD of all NA lakes and reservoirs. The RGRB model performed well during calibration ($R^2 = 0.81$) and validation ($R^2 = 0.78$, MAPE = 30.85 %). This model also exhibited stable and reliable performances regardless of the Landsat sensors (TM, ETM+, and OLI), despite spectral configuration differences among these sensors. RGRB was implemented to generate SDD maps for all lakes and reservoirs (water surface area ≥1 ha) across NA in 2019. More than 2.9 million lakes and reservoirs were mapped with Landsat OLI images, resulting in an average SDD of 3.84 ± 1.77 m. A strong positive relationship between average SDD and log-transformed water surface area ($R^2 = 0.80$, $p < 0.001$) indicated that large lakes and reservoirs tend to be more transparent than small ones. Latitudinal variations were found in the water clarity gradient, with maximum SDD recorded at the 35°N–60°N latitude and lower SDD at the 10°N–30°N latitude. This model can be implemented using the Google Earth Engine platform to derive SDD for NA lakes and reservoirs at annual or even seasonal time steps to assess water eutrophication variation in both time and space at the continental scale.

1. Introduction

Inland waters support high levels of biodiversity (Balian et al., 2007; Grantham et al., 2019) and provide several ecosystem services beneficial to human well-being (e.g., drinking water, irrigation, fisheries, and creation) (Alcamo et al., 2007; Brauman et al., 2013). However, inland waters, particularly relatively static water bodies such as lakes and reservoirs, are vulnerable to the synergistic effects of multiple environmental pressures, including nutrient enrichment, organic and inorganic pollution from anthropogenic activities, and climate change (Bergström and Karlsson, 2019; Sterner et al., 2020; Zhang et al., 2020). In many regions, the ecosystems of lakes and reservoirs are increasingly impacted by ecologically significant events such as harmful algal blooms (Mishra et al., 2020). The sensitivity of lakes and reservoirs to climate change, land use, and other environmental disturbances has attracted growing attention in recent years. Therefore, there is a pressing need to

* Corresponding author.
E-mail address: liuge@iga.ac.cn (G. Liu).
[1] Equal contribution to the manuscript.

https://doi.org/10.1016/j.isprsjprs.2022.09.014
Received 15 April 2022; Received in revised form 12 August 2022; Accepted 16 September 2022
Available online 17 October 2022

develop tools for monitoring freshwater ecosystems and understanding their responses to current and future environmental changes (Shen et al., 2020).

Water clarity is an effective proxy for aquatic ecosystem health. It has been used to evaluate lake and reservoir trophic status due to its strong link with algal abundance (Chl-a), total suspended matter (TSM), total nitrogen (TN), and total phosphorus (TP) (Carlson, 1977; Song et al., 2014). The Secchi disk depth (SDD) is commonly used to express water clarity (Tyler, 1968; Lee et al., 2016), and its widespread adoption stems from its low cost, simplicity, and ease of operation (Kloiber et al., 2002; Song et al., 2020). However, for large regional-scale studies, the conventional SDD method is limited in the number of lakes and reservoirs that can be investigated and the geographic extent of such studies. This consideration is particularly relevant for lakes and reservoirs situated in remote areas, where accessibility can be challenging (Olmanson et al., 2008; Song et al., 2020). Further, measurements frequency, the cost of field campaigns, and the number of lakes and reservoirs that can be monitored simultaneously are some of the other limitations of conventional SDD measurement approaches (Sayers et al., 2015).

Water clarity has a direct correlation with optically-active constituents (OACs) that can be present in waters, e.g., phytoplankton, non-algal particles (NAP), and colored dissolved organic matter (CDOM) in the water column (Song et al., 2012; Lee et al., 2016). Thus, optical remote sensing has been used to estimate SDD through its strong link with OACs, which can affect the water-leaving radiance signal and can be detected by optical sensors onboard satellite platforms (Boland, 1976; Lillesand et al., 1983; Kloiber et al., 2002; Shen et al., 2020). Over the past four decades, optical remote sensing has been demonstrated as an effective tool for monitoring water quality characteristics of lakes and reservoirs at local, regional, and global scales (Kutser, 2004; Kloiber et al., 2002; Duan et al., 2008; Sayers et al., 2015). Furthermore, satellite remote sensing reduces the cost of labor-intensive environmental monitoring programs by combining limited in situ measurements with models that capture the spatial and temporal dimensions of relevant environmental processes (Boland, 1976; Lillesand et al., 1983; Olmanson et al., 2008). Among the several satellite systems (e.g., SeaWiFS, Terra, Aqua/MODIS, MERIS, IRS-LISS, and Sentinel-2A) used for water quality monitoring, the Landsat satellite sensor series has particularly been useful for the long-term assessment of biogeochemical characteristics of inland waters (Alföldi and Munday Jr., 1978; Duan et al., 2008; Song et al., 2020). Several studies have established reliable empirical relationships between Landsat imagery and ground observations of water quality parameters, including Chl-a, SDD, and TSM (Zheng et al., 2015; Watanabe et al., 2015; Liu et al., 2019) at a local or regional scale.

Since 1972, the Landsat sensors have provided the longest record of water resources observation from space (Alföldi and Munday Jr., 1978; Lillesand et al., 1983; Loveland and Dwyer, 2012; Page et al., 2019). Its medium spatial resolution (30–60 m) makes it suitable for SDD estimates in large and small inland water bodies . In most cases, empirical models have been developed between Landsat top of atmospheric (TOA) surface reflectance and in situ SDD measurements (Song et al., 2020). Several previous studies have described effective methods to evaluate the water clarity of lakes and reservoirs using Landsat TM and ETM+ imagery (Kloiber et al., 2002; McCullough et al., 2012; Courville et al., 2014). However, numerous models are constrained by poor geographical and temporal transferability (Kloiber et al., 2002; Olmanson et al., 2008). Water clarity models are often limited to regional lake and reservoir studies, and in most cases, models need to be tuned with co-concurrent in situ SDD and satellite overpasses within a specific time window (Kloiber et al., 2002; Olmanson et al., 2008). For some specific case studies, robust algorithms have been used with relative success to retrieve SDD using Landsat OLI imagery over large inland water bodies (e.g., the Three Gorges reservoir and Lake Dongting in China) (Zheng et al., 2015; Shen et al., 2020). To improve SDD modeling accuracy, McCullough et al. (2012) have combined Landsat spectral variables with hydrological features of lakes and reservoirs occurring in a catchment. Lee et al. (2016) developed a semi-analytical model to improve both the accuracy of water transparency estimates from remote sensing data and the temporal transferability of the model. The newly developed semi-analytical scheme was applied to Landsat OLI data to obtain a high-spatial-resolution map of water clarity (Lee et al., 2016). The method has been tested in lakes from other regions with some success (Rodrigues et al., 2017). It has also been modified for application to turbid lakes and reservoirs in the mid-lower reaches of the Yangtze River Basin (Feng et al., 2019). Although researchers have developed different retrieval algorithms to estimate SDD, these tend to be lake-specific due to variations in OAC composition. Moreover, the application of semi-analytical and analytical models is often limited by the unavailability of proper initialization parameters or restricted bio-optical parameters for model parameterization (Sayers et al., 2015). Empirical models are often used to derive large-scale SDD estimates (Olmanson et al., 2008; Song et al., 2020).

Recent progress has been made to utilize moderate and coarse resolution satellite data (e.g., SeaWiFS, MODIS, MERIS, or OLCI) for frequent and large-scale monitoring of lacustrine SDD (Binding et al., 2015; Liu et al., 2019; Shen et al., 2020). Most past studies have focused on lakes and reservoirs with surface areas in the 10–100 km^2 range (Liu et al., 2019), and relatively few efforts have been devoted to the application of remotely-sensed imagery data to monitor water clarity of small lakes at regional and continental scales (Bonansea et al., 2015; Song *et al.*, 2022b). A notable example of such applications is the work of Olmanson et al. (2008), involving long-term (~20 years) monitoring of SDD and trends in water clarity in thousands of Minnesota lakes using Landsat data. However, their modeling approach requires concurrent in situ measurements of SDD for model tuning and parameterization, which may limit its potential use for estimating SDD in lake and reservoir regions where extensive in situ measurements are not available. Thus, there is a need for a stable and less data-intensive model for SDD that can extend the application of Landsat data to study water quality variations in both time and space (Olmanson et al., 2008; Bonansea et al., 2015; Ren et al., 2018; Song *et al.*, 2022b). Studies indicated that the Landsat TOA reflectances provided by the Google Earth Engine (GEE) have great potential for regional and national scale assessment of lake and reservoir water quality (Wang and Gordon, 2018; Vanhellemont and Ruddick, 2018; Song et al., 2020); however, continental and global scale analyses of water quality trends using these tools have not been explored yet. Although a few studies have examined SDD variations at continental and global scales, these assessments were limited to large surface area lakes and reservoirs (Wang and Gordon, 2018; Liu et al., 2019). Thus, the primary purpose of this study is to establish a robust model for large-scale mapping of SDD in small lakes and reservoirs using Landsat TOA reflectance on the GEE. The specific objectives are to (1) collect and assemble in situ SDD data for lakes and reservoirs across North America (NA) and match the measured data with spectral information acquired from Landsat series sensors to derive an SDD model; (2) evaluate various models and select the model with the best performance to estimate SDD in lakes and reservoirs with surface area $\geq$ 1 ha across NA, and (3) examine the spatial variation of SDD in lakes and reservoirs across NA.

2. Materials and methods

2.1. Study area

Lakes and reservoirs cover only 3–4 % of the global non-glaciated terrestrial surface (Verpoorter et al., 2014). Lakes and reservoirs are unevenly distributed, and about 43.5 % of the permanent lakes and reservoirs occur in NA (Pekel et al., 2016). Although the total area of permanent inland waters in the United States has increased by 0.5 % since 1984, drought and increased water demand have reduced their areal extent by 33 % (or ~6000 km^2) in six western states (Pekel et al., 2016). In Mexico, the reduction in water availability as a consequence of

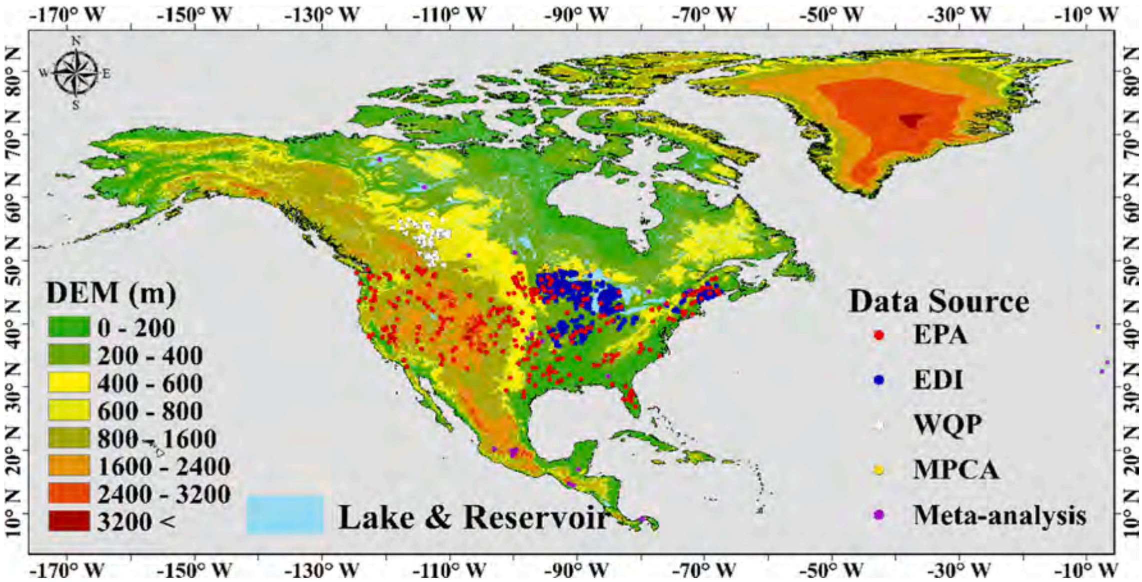

Fig. 1. Distribution of SDD-measuring stations across North America. Red points denote EPA dataset, blue points denote EDI dataset, white points denote WQP, orange points denote MPCA dataset, and purple points denote data retrieved from the literature. (For interpretation of the references to colour in this figure legend, the reader is referred to the web version of this article.)

Table 1
Comparative performance of some published models for retrieving SDD based on Landsat imagery data. All these models were calibrated using the calibration dataset (Model expressions) and validated using the calibration dataset.

Author	Model expressions	Sensor	Equations	R^2	N	RMSE	MAPE
Richard (1986)	Ln (SDD) = −2.10*ln(G)-0.18	TM	y = 0.62x + 1.99	0.50	1668	1.26	55.10
Allee (1999)	Ln (SDD) = −2.10*ln(G) −0.003*ln(R) + 0.0001*ln(SWIR) −0.185	TM	y = 0.61x + 0.90	0.56	1653	1.08	36.06
	Ln (SDD) = −80.67 *R + 484.09*(R)^2 −237.92 *(R)^3 + 8.06	TM	y = −0.26x + 7.62	0.34	1668	6.53	600.63
Kloiber (2002)	Ln (SDD) = −5.87*(B/R) + 1.08*B + 8.08	TM	y = 0.75x + 1.38	0.75	1668	0.94	31.43
Stacy (2002)	Ln (SDD) = −5.86*(B/R) + 1.083	ETM+	y = 0.69x + 1.67	0.69	371	1.69	36.14
Hellweger (2004)	Ln (SDD) = 0.74*R + 1.37	TM	y = 0.62x + 2.07	0.62	1668	1.10	40.61
Guan (2011)	Ln (SDD)) = −6.31*(B/R) + 3.83*R + 8.225	TM	y = 0.75x + 1.38	0.75	1668	0.94	31.38
Fuller (2011)	Ln (SDD) = 41.22*B −28.40 *G −35.33*R + 5.11	TM	y = 0.74x + 1.43	0.74	1668	0.97	31.28
Page (2018)	Ln (SDD) = −4.29 *(B/R) + -9.29*(G) + 7.74	OLI	y = 0.75x + 1.37	0.75	276	0.66	35.02
Song (2022)	Ln (SDD) = −5.30*(R/B) + -4.29*(B/G) + 8.21	TM	y = 0.86x + 0.37	0.82	1668	0.62	30.45

Table 2
Calibration and evaluation of performance (using RMSE, MAPE, and Bias) of SDD models established using various modeling approaches. Abbreviations: R represents red band, B represents blue band, and G represents the green band in different Landsat sensors.

Sensor	Equation	R^2	RMSE	MAPE	Bias
Landsat OLI	LN(SDD) = −29.7*R + 6.10	0.39	0.65	39.87	0.45
	LN(SDD) = −5.24*R/B + 7.48	0.70	0.51	38.22	0.34
	LN(SDD) = 5.688*B/G − 2.50	0.81	0.41	16.85	0.22
	LN(SDD) = −0.76*R/B + 5.11*B/G − 1.37	0.82	0.40	16.15	0.23
Landsat ETM+	LN(SDD) = −31.45*R + 6.71	0.61	1.17	37.65	0.76
	LN(SDD) = −5.84*R/B + 8.01	0.67	1.03	44.36	0.70
	LN(SDD) = 5.05*B/G − 1.55	0.66	1.29	31.84	0.70
	LN(SDD) = −2.36*R/B + 3.65*B/G + 1.48	0.81	0.96	26.11	0.54
Landsat TM	LN(SDD) = −31.28*R + 6.88	0.55	1.10	40.25	0.83
	LN(SDD) = −5.58*R/B + 8.07	0.66	1.03	33.15	0.76
	LN(SDD) = 4.25*B/G − 0.45	0.67	1.08	29.13	0.71
	LN(SDD) = −2.81*R/B + 2.73*B/G + 2.96	0.82	0.75	21.63	0.52

climate change not only compromises water reliability for industries and agriculture but also challenges the provision of drinking water, a most basic human need (Gradilla-Hernández et al., 2019). Canada is endowed

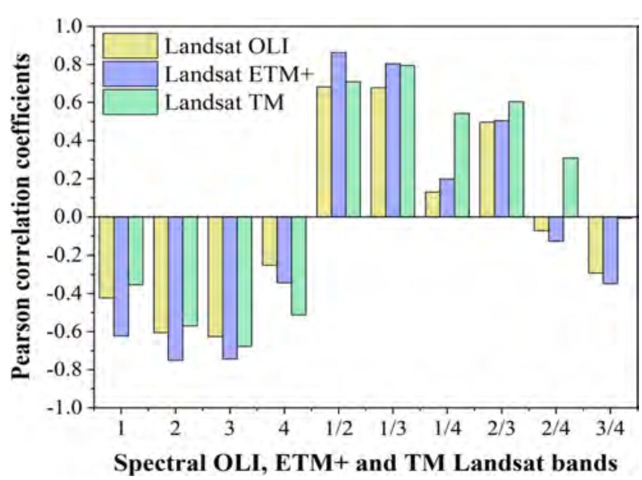

Fig. 2. Pearson correlation coefficients of the relationships between SDD versus spectral bands and band ratios of Landsat sensors. Blue, Green, Red, and NIR for OLI bands 2, 3, 4, and 5; Blue, Green, Red, and NIR for Landsat TM/ETM+ bands 1, 2, 3, and 4. (For interpretation of the references to colour in this figure legend, the reader is referred to the web version of this article.)

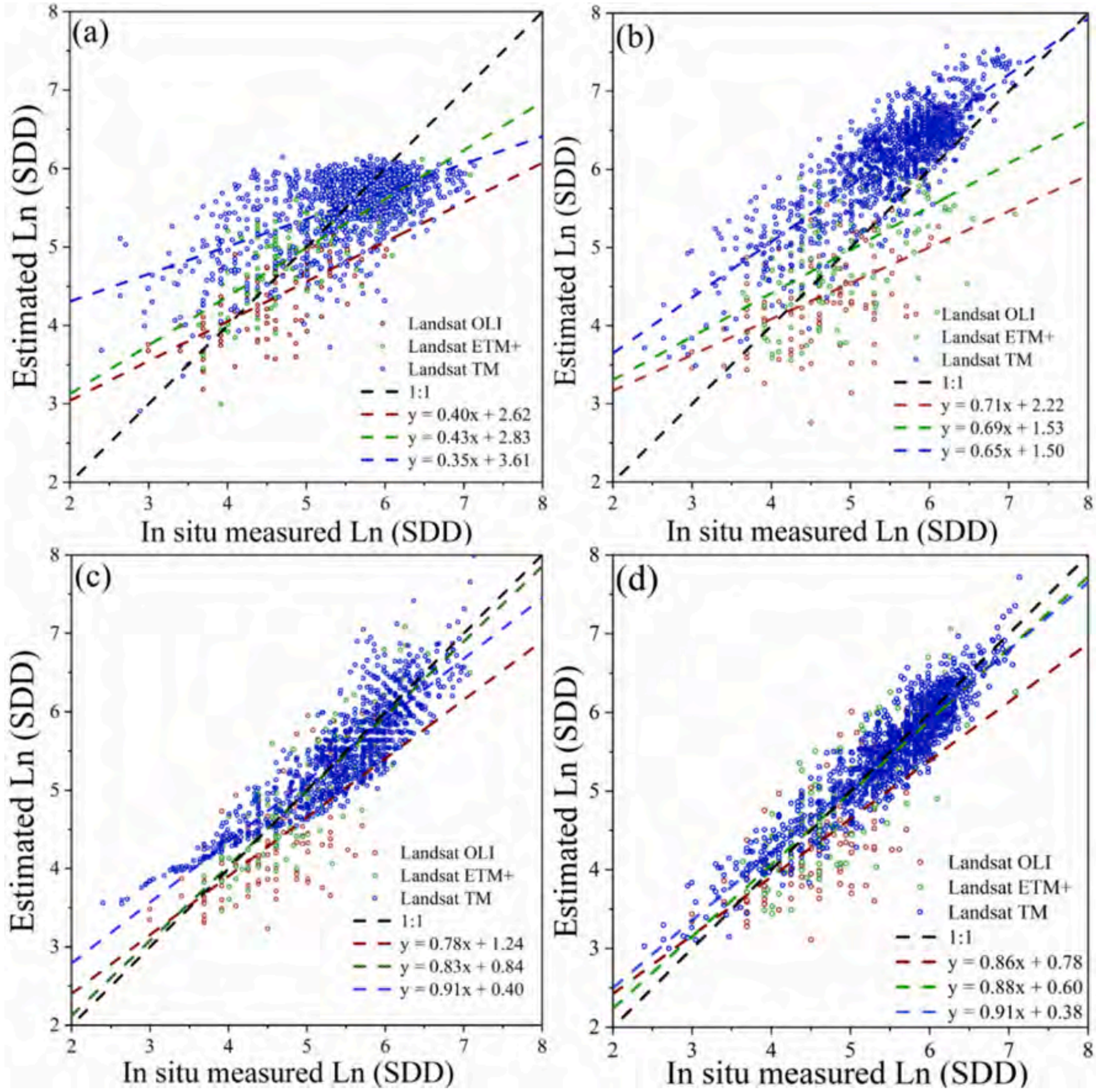

Fig. 3. Scatter plots of in situ SDD (ln-transformed) and estimated SDD (ln-transformed) using different modeling approaches and spectral data acquired with different Landsat sensors. (a) Landsat red model, (b) Landsat red/blue band ratio model, (c) Landsat blue/green band ratio model, and (d) Landsat red/blue and blue/green band ratios using a multi-step model. (For interpretation of the references to colour in this figure legend, the reader is referred to the web version of this article.)

Table 3
Model calibration with different modeling approaches and evaluation of model performance (using RMSE, MAPE, and Bias) with pooled dataset acquired with different Landsat sensors.

Band	Equation	R^2	RMSE	MAPE	Bias
R	LN(SDD) = −34.56*R + 6.96	0.57	1.10	40.82	0.82
R/B	LN(SDD) = −5.90*R/B + 8.17	0.68	1.02	34.94	0.74
B/G	LN(SDD) = 4.57*B/G − 0.92	0.73	1.10	29.54	0.70
R/B + B/G	LN(SDD) = −2.74*R/B + 3.01*B/G + 2.51	0.81	0.76	21.77	0.51

with the most freshwater per capita in the world, much of it located in northern lakes and rivers draining north. However, over 90 % of the Canadian population lives in a narrow band along the southern border, where water is relatively less abundant. Despite Canada's low population density and large land mass, significant water pollution problems have been identified in some areas (Binding et al., 2015). There are more than 2.9 million lakes and reservoirs with an area ≥ 1 ha in NA; however, only a very small proportion of these (about 1227 lakes and reservoirs) are regularly and consistently monitored (Olmanson et al., 2008; Brezonik et al., 2015; Binding et al., 2015).

2.2. In situ SDD datasets

To establish robust models for lake and reservoir clarity mapping in NA (surface area ≥ 1 ha), in situ SDD datasets were assembled from lakes and reservoirs located in different geographic regions, morphology, hydrographic and hydrochemical conditions (including OACs) (Brezonik et al., 2015; Song et al., 2020). SDD data were collected from various sources. The first SDD dataset was collected from the US Environmental Protection Agency (US-EPA) (downloaded from the EPA's STORET water quality data repository; https://www.epa.gov/storet/). As part of routine aquatic environmental monitoring work, in situ SDD from water bodies across the conterminous US were collected by the US-EPA in 2007 and 2009. The second major SDD dataset was from the Environmental Data Initiative (EDI, https://portal.edirepository.org/nis/home.jsp). This National ScienceFoundation-funded project actively promotes

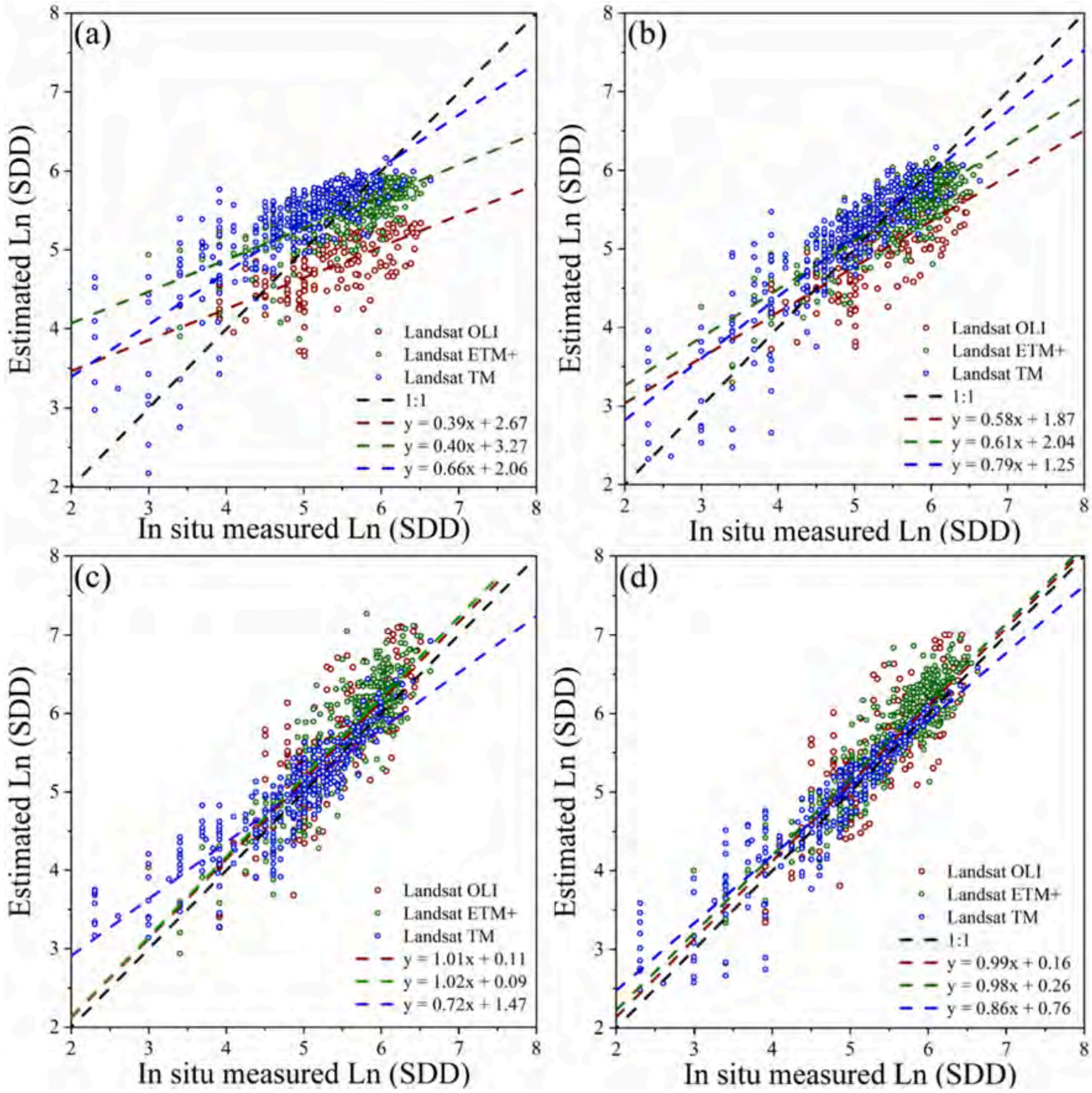

Fig. 4. Scatter plots for comparing validation data with SDD estimates are obtained with the different modeling approaches listed in Fig. 3. Results are presented for different Landsat sensors and models: (a) Landsat red model, (b) Landsat red/blue band ratio model, (c) Landsat blue/green band ratio model, (d) Landsat red/blue and blue/green band ratios using a multi-step regression model. (For interpretation of the references to colour in this figure legend, the reader is referred to the web version of this article.)

and enables the curation and re-use of environmental data. Measured SDD data from publicly-funded research is available through this website (https://environmentaldatainitiative.org/). The third SDD dataset was from the surface water monitoring stations of the Minnesota Pollution Control Agency (MPCA, https://webapp.pca.state.mn.us/wqd/surface-water). The MPCA monitors environmental quality, offers technical and financial assistance, and enforces environmental regulations.

The last SDD dataset was from a meta-analysis of relevant published literature, which was mainly used to validate model performance. We downloaded all the literature published in the past three decades (1990–2019) using ISI Web of Science with lake, reservoir, water quality, clarity, transparency, and SDD as keywords. Altogether, 420 relevant articles were identified, and the SDD record was retrieved along with ancillary information presented in each article. For some articles, the information provided was inadequate; therefore, we only retained SDD records that also included collection date and geo-location (Lat-longitude). When in situ SDDs were reported for multiple locations within a lake and reservoir for a known time frame, the average SDD was taken to represent the water clarity status of the whole lake and reservoir. In this case, the average Landsat TOA reflectance value was also used.

Altogether, we obtained 109,741 SDD measurements from EDI, WQP, EPA, and MPCA for lakes and reservoirs across NA. The SDD observations spanned from 1984 to 2019. For most of the monitoring stations, SDD observations were from the ice-free season (June-October). Eventually, 3235 SDD samples were matched up with Landsat imagery acquired within ±7 days of the measurement and collected by different Landsat sensors (TM, ETM+, and OLI) (see Fig. 1).

2.3. Landsat images matchups with in situ SDD

GEE stores a petabyte archive of Earth Observations data that provides and relates data using an efficient processing software coded in Python and describes these data in API format (Gorelick et al., 2017). Landsat imagery data acquired by different sensors (e.g., TM, ETM+, and OLI) were available and processed with the GEE platform. Landsat calibrated TOA Tier 1 collections for Landsat TM, ETM+ and OLI were

Table 4
Model validation of the algorithms listed in Table 2 and evaluation (using RMSE, MAPE, and Bias) of the relationships between in situ and Landsat predicted SDD.

Sensor		In situ vs Landsat Pred.	R^2	N	RMSE	MAPE	Bias
Landsat OLI	R	y = 0.39x + 2.67	0.43	180	1.82	54.03	1.34
	R/B	y = 0.58x + 1.88	0.58	180	1.62	46.29	1.14
	B/G	y = 1.01x + 0.11	0.51	180	2.12	44.18	1.34
	R/B + B/G	y = 0.99x + 0.16	0.54	180	1.47	42.42	1.06
Landsat ETM+	R	y = 0.40x + 3.27	0.51	411	1.83	38.76	0.97
	R/B	y = 0.61x + 2.03	0.68	411	1.35	32.53	0.97
	B/G	y = 1.02x + 0.10	0.60	411	1.21	41.05	1.24
	R/B + B/G	y = 0.98x + 0.26	0.68	411	1.05	30.18	0.89
Landsat TM	R	y = 0.66x + 2.06	0.65	637	0.92	84.37	0.77
	R/B	y = 0.78x + 1.25	0.78	637	0.62	44.53	0.47
	B/G	y = 0.72x + 1.47	0.79	637	0.48	37.91	0.36
	R/B + B/G	y = 0.86x + 0.76	0.86	637	0.31	25.39	0.24

Table 5
Model validation of the algorithms listed in Table 3 and evaluation (using RMSE, MAPE, and Bias) of the relationships between in situ and Landsat-predicted SDD with pooled validation dataset acquired with different Landsat sensors.

Models	In situ vs Landsat pred.	R^2	RMSE	MAPE	Bias
R	y = 0.50x + 2.71	0.43	1.37	63.21	0.92
R/B	y = 0.68x + 1.69	0.58	1.06	38.23	0.69
B/G	y = 0.87x + 0.81	0.69	1.14	41.34	0.80
R/B + B/G	y = 0.94x + 0.42	0.78	0.96	30.85	0.61

used for this study (Chander et al., 2009). A customized JavaScript cloud masking and compositing script algorithm were implemented in GEE to suppress different types of clouds and noises and to generate a multi-spectral composite cloud-free image for visual inspection of imagery quality for further implementation of SDD estimate.

Matching up Landsat overpasses with in situ SDD is a key step in the modeling effort. The time window for matching Landsat TOA and in situ observations was set to ±7 days to ensure sufficient matchups (Olmanson et al., 2008; Song et al., 2020). The other criterion that needs to be considered is cloud contamination, which affects the images being selected for SDD mapping (Chander et al., 2009). Here, we set the threshold for images with cloud coverage <10 % of the lake and reservoir water surface area. When this threshold was established, the pixels affected by clouds or haze were manually masked and removed. Landsat images were selected to match up with in situ SDD according to these two criteria noted above (Onderka and Pekárová, 2008). These selected Landsat TOA meeting these criteria were downloaded from the GEE platform. The ArcGIS software package was used to extract the Landsat TOA reflectance at the latitude and longitude of the sampling points. The mean value of a 3 × 3 pixels box centered at an in situ measurement site was used as the final Landsat reflectance value, which was eventually used for model calibration and validation. Altogether, 3235 sampling points were matched in NA, including 290 sampling points from Landsat OLI images, 690 sampling points from Landsat ETM+ images, and 2255 sampling points from Landsat TM images. The number of data for the three sensors (TM, ETM+, and OLI) in the validation dataset is 834, 280, and 111, respectively. The number of data for the three sensors (TM, ETM+, and OLI) in the calibration dataset is 1421, 410, and 179, respectively. A total of 574 matchups were produced using the Landsat 7 ETM+ SLC-off data (the Landsat 7 ETM+ images that had gaps collected after May 31, 2003). The gaps region were eliminated in producing matchups and mapping remote sensing SDD products of North America.

2.4. The simulated dataset

2.4.1. Data simulation description

The simulated dataset CoastColour Round Robin datasets (CCRR) was employed in this study. The CCRR was simulated using HydroLight version 5.0 by inputting the variable parameters as shown in Nechad et al. (2015), which included the specific absorption coefficient of phytoplankton (a^*_{ph}), the specific coefficient of detritus (a^*_d), the spectral slope of a^*_d (S_d), the spectral slope of CDOM (denoted as S_g), the specific scattering coefficient of detritus (b^*_d), the spectral variation of the beam attenuation coefficient for phytoplankton (γ_{Chl}), the spectral variation of the beam attenuation coefficient for detritus (γ_d), the atmospheric, air-sea interface, and sun and viewing angle parameters. A total of 5000 triplets of Chl*a* (range: 0.02–214.41 mg m^{-3}), detritus concentrations (range: 0.002–492.78 mg L^{-1}) and CDOM absorption at 443 nm ($a_g(443)$) (range: 0.002–14.84 m^{-1}) were generated in the CCRR dataset. The wide range of Chl*a* and detritus concentrations and $a_g(443)$ implied that this simulated dataset could represent most types of inland waters. The simulated parameters of CCRR include total absorption (a), total backscattering coefficient ($b_b(\lambda)$), phytoplankton absorption coefficient ($a_{ph}(\lambda)$), water-leaving reflectance ($R_w(\lambda)$), diffuse downwelling irradiance attenuation spectra ($k_d(\lambda)$), and photosynthetically available radiation (PAR).

2.4.2. Calculation of simulated $\rho_{TOA}(\lambda)$ and SDD

First, the simulated remote sensing reflectance ($R_{rs}(\lambda)$) was obtained using $R_w(\lambda)$ in the CCRR (the sun and viewing zenith angle were both 0°, the sun and viewing zenith angle were 0° and 90°, respectively) divided by π. Second, the simulated Landsat OLI remote sensing reflectances ($R_{rs}(\lambda)$) in the ultra-blue, blue, green, and red bands derived by applying each Landsat OLI's spectral response function (SRF) were downloaded from the website of the United States Geological Survey (USGS) (https://landsat.usgs.gov/instructions.php). Third, the simulated Rayleigh and aerosol parameters, including the Rayleigh reflectance (ρ_r), the aerosol reflectance (ρ_a), the total upward diffuse atmospheric transmission ($t_u(\lambda)$) and the total downward diffuse atmospheric transmission ($t_d(\lambda)$) were obtained using the Second Simulation of the Satellite Signal in the Solar Spectrum (6SV) and its python interface (Py6S) with the same sun and viewing angles described above for different values of aerosol optical thickness loadings ($\tau_a(\lambda)$) (indexed by $\tau_a(\lambda)$ at 550 nm ($\tau_a(550)$), $\tau_a(550)$=0.0–0.5, increments of 0.01) (Kotchenova et al., 2006; Kotchenova and Vermote, 2007). The aerosol type was fixed as the commonly used "Continental" models in the atmospheric correction of inland waters. Then, TOA reflectance ($\rho_{TOA}(\lambda)$) can be calculated using the simulated Landsat OLI $R_{rs}(\lambda)$ and simulated Rayleigh and aerosol parameters according to Eq. (1).

$$\rho_{TOA}(\lambda) = \rho_a(\lambda) + \rho_r(\lambda) + t_u(\lambda)t_d(\lambda)*\pi*R_{rs}(\lambda \tag{1}$$

CCRR did not provide the SDD data. The semi-analytical inversion model proposed by Lee et al. (2016) was used to simulate SDD. Feng et al. (2019) demonstrated that this model performs well in retrieving SDD in lakes and reservoirs with various optical properties on a large regional scale. In this study, we used this model to simulate the SDD data described in Eq. (2).

$$\mathrm{SDD} = \frac{1}{2.5\min(k_d(Blue), k_d(Green), k_d(Red))}*\mathrm{In}\left(\frac{|0.14 - R^{pc}_{rs}|}{C^r_t}\right) \tag{2}$$

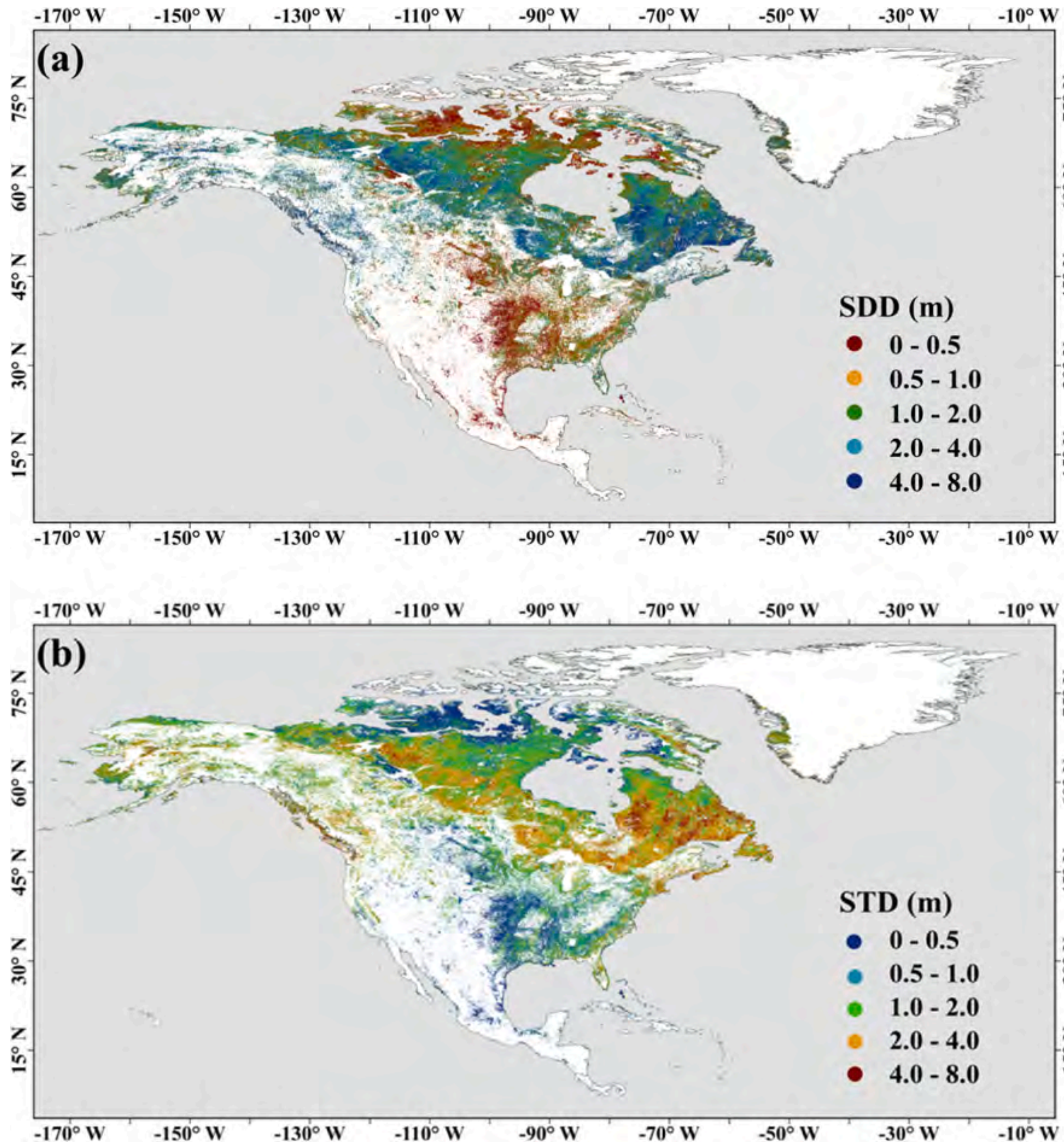

Fig. 5. Mean distribution of SDD (a) and standard deviation of SDD (b) in lakes and reservoirs (water surface area $\geq$ 0.01 km^2) across North America derived from OLI images acquired in 2019. For a given lake and reservoir, mean SDD was computed based on all the pixels within the lake and reservoir boundary as delimited by the lake and reservoir's mask shape file.

where C_t^r (equals to 0.013 sr^{-1}) is the detection threshold of the human eye in air, $k_d(blue)$, $k_d(green)$, and $k_d(red)$ are the Landsat OLI $k_d(\lambda)$ at blue, green, and red bands calculated by the simulated $k_d(\lambda)$ in CCRR and applying each Landsat OLI's spectral response function (SRF), R_{rs}^{pc} is taken as the $R_{rs}(\lambda)$ value corresponding to the wavelength with the minimum $k_d(\lambda)$ at blue, green, and red bands. The simulated SDD values ranged from 0.08 to 36.05 m, with an average of 5.49 m.

2.5. Algorithm development

Model development is the key step in successfully using satellite data for large-scale mapping of inland waters SDD. First, we conducted a correlation analysis between in situ SDD and corresponding Landsat TOA reflectance. All possible band ratio combinations and original spectral band reflectance were tested (Kloiber et al., 2002). The spectral bands and band ratios that yielded higher correlation coefficients were used as candidate variables for SDD modeling. Further, these models with good performance proposed by previous case studies were also examined to test their effectiveness in our datasets (Lathrop and Lillesand, 1986; Allee and Johnson, 1999; Kloiber et al., 2002; Nelson et al., 2002; Hellweger et al., 2004; Guan et al., 2011; Page et al., 2019). These models included linear, cubic equation, and log transformations; their modeling parameters and model performance are presented in Table 1.

We divided the in situ SDD into two groups to calibrate and validate the models. The calibration dataset included 2010 samples, and the validation dataset included 1225 samples. To determine which spectral band or band ratio was the best predictor of SDD, Pearson correlation and backward multiple regression analysis were carried out between log-transformed in situ SDD and TOA reflectance of TM, ETM+ and OLI bands of the calibration group (also see Table 2). We used root mean square error (RMSE), mean absolute percentage error (MAPE), and Bias to assess model accuracy. The formula for RMSE and MAPE are:

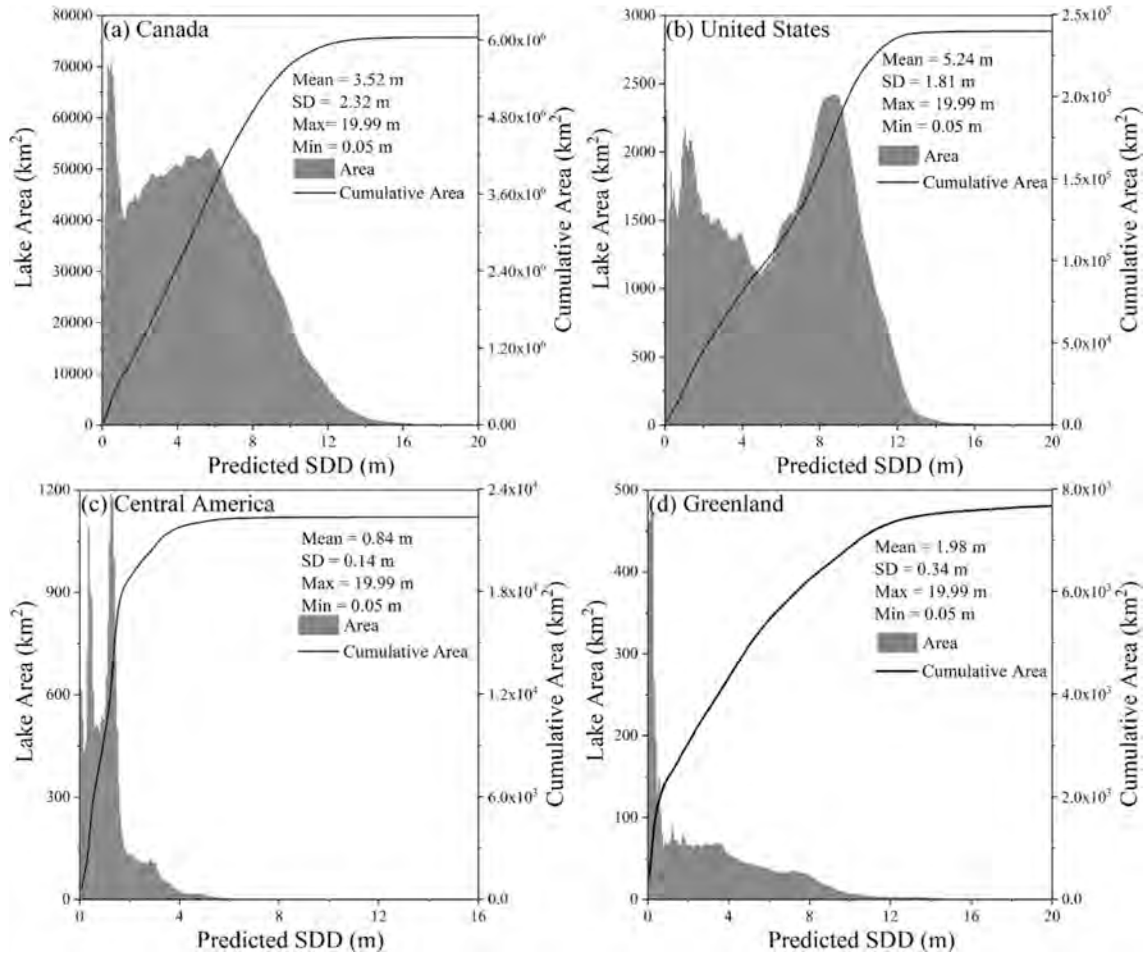

Fig. 6. Distribution of SDD in relation to lake and reservoir areas in different countries or regions in North America. The cumulative area of lakes and reservoirs is also displayed. Descriptive statistics were computed using pixel values for all lakes and reservoirs in a given country or region.

$$\mathbf{RMSE} = \sqrt{\frac{\sum_{i=1}^{N}(\mathbf{y}_i^{'} - \mathbf{y}_i)^2}{\mathbf{N}}} \quad (3)$$

$$\mathrm{MAPE} = \frac{100\%}{\mathrm{N}}\sum_{i=1}^{N}\left|\frac{y_i^{'} - y_i}{y}\right| \quad (4)$$

where N is the total number of samples, where y_i and $y_i^{'}$ are the in situ SDD, and model predicted SDD values.

2.6. Lake and reservoir mask generation for NA

In this study, continental lake and reservoir surface area boundaries from NA were delineated by using Landsat OLI imagery data mainly acquired in 2019. The cloudless Landsat TOA image of each path and row close to 2019 was downloaded and processed to calculate the Modified Normalized Difference Water Index (MNDWI), calculated as follows:

$$MNDWI = (R_{green} - R_{swir})/(R_{green} - R_{swir}) \quad (5)$$

where R_{green}, R_{swir} are the TOA reflectance in the green band and the short-wave infrared (SWIR) bands, respectively. Firstly, we used MNDWI, Tasseled Cap Transformation (TC), and a density slicing with a multi-threshold approach to building a decision tree for retrieving water body boundaries using the Environment for Visualizing Images (ENVI) software package (Feyisa et al., 2014; Song et al., 2020). The MNDWI was firstly used to preliminary divide the pixels into two classes, non-water, and water, with a certain MNDWI value between 0.03 and 0.20 determined by visual interpretation. Ludwig et al. (2019) illustrate that MNDWI may be difficult to distinguish the wetlands and waters for some humid climatic regions, e.g., Mississippi Delta. For this situation, the density slicing results of the wetness band of the tasseled cap transformation were also used to eliminate the wetlands misclassified as water pixels visual interpretation. The extracted water bodies were then converted into polygons with contiguous pixels and stored in shape files using ArcGIS 10.4 (ESRI Inc. Redlands, CA, USA). The water pixels of lakes nearby offshore, which the substrates may influence, were masked using the method described in our previous work (Tao et al. 2022). In order to avoid the influence of adjacent land on water bodies, a 2-pixel buffer inward of water boundary was removed for lakes with an area $\leq$1 km^2 and 5-pixel for lakes with an area $>$1 km^2. We divided water bodies into lakes, reservoirs, and rivers according to their shoreline features and also based on the Global Reservoirs and Dams database (Lehner et al., 2011) and high-resolution images from Google Earth (Song et al., 2020). Secondly, we exported the continental lakes and reservoirs into shapefiles. Finally, all lakes and reservoirs with an area $\geq$ 1 ha were determined as the initial study area (Fig. S1) and used to mask water clarity map results.

2.7. Continental SDD mapping and statistical analysis

For the Landsat standard swath (scene), 2335 paths/rows are needed to cover the lakes and reservoirs all over the NA continent. The 2019 Landsat OLI image was filtered such that only images with $<$10 % cloud covers were used to derive the SDD spatial distribution in NA. Then,

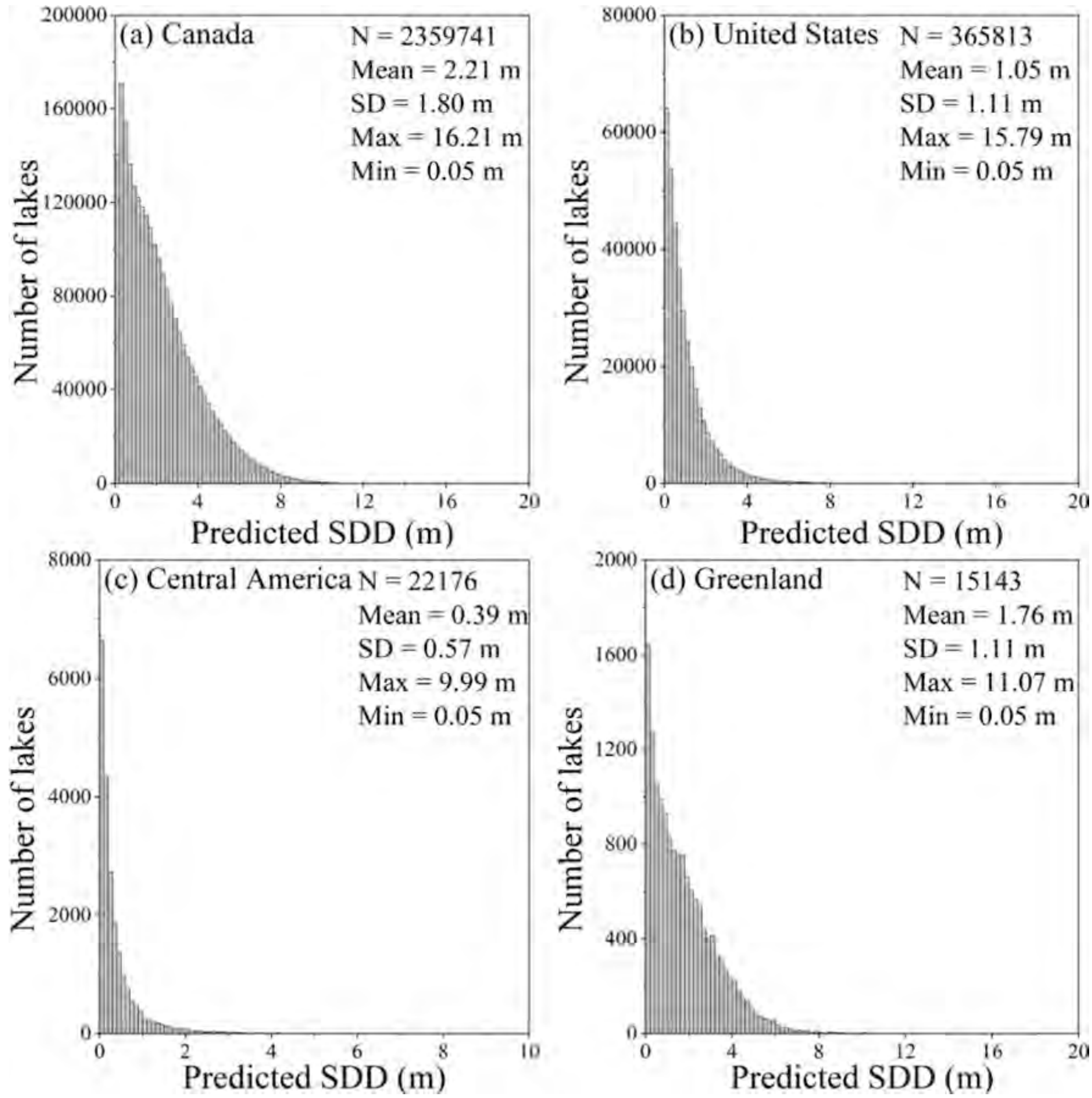

Fig. 7. Histogram of the distribution of mean SDD for lakes and reservoirs in different parts of North America, (a) Canada Lake Region, (b) United States Lake Region, (c) Central America, and (d) Greenland. Descriptive statistics were computed without consideration of lake and reservoir size.

water bodies with an area ≥ 1 ha were selected, and the SDD value was masked out for further analysis and mapping. Besides, the mean SDD maps using TM (in 2001) and ETM + (in 2012) alone were also produced, as shown in Fig. S5 and Fig. S6 in the Support Materials Section.

After generating the SDD map for inland waters, we conducted statistical analyses of SDD in different countries and geographic zones to explore the spatial pattern for water clarity. We calculated the averaged SDD for each lake and reservoir by using all qualified images during the ice-free period in 2019 and then merged the annual mean SDD of each lake and reservoir. We also compared the spatial variation of SDD in different countries and the longitudinal and latitudinal variations of SDD. Further, we also conducted statistical analysis between Landsat predicted and in situ SDD in some specific lakes and reservoirs, where long-term SDD records are available, aiming to test the continental model performance for tracking temporal SDD variations.

3. Results

3.1. Models linking SDD and Landsat observations

A strong relationship was found between in situ SDD and Landsat data in the red band and the blue-to-green and blue-to-red band ratios (Table 2 and Fig. 2). The strength of the relationships, as expressed by high Pearson correlation coefficients, suggested that these variables can be used to construct suitable models for SDD monitoring. We developed empirical models based on these spectral bands (red band and the band ratios of blue-green and blue-red) and band combinations using simple regression or multi-step regression analysis to retrieve SDD from Landsat data for lakes and reservoirs across the whole NA continent. Results showed that regression models based on only the red band TOA reflectance had lower accuracy (Fig. 3a) and generally led to the underestimation of SDD (slope between 0.35 and 0.40 with the ln-transformed SDD data) for imagery acquired with Landsat sensors (TM, ETM+, and OLI). Further, the intercept values (range: 2.62–3.61 m) also suggested marked variation among images acquired by different Landsat sensors. The band ratio model based on the red-blue spectral ratio has been widely applied for SDD estimation in lakes and reservoirs from different regions. The scatterplot between in situ measured and Landsat predicted SDD indicated that the red-blue band ratio model significantly improved in comparison to the red band model (Fig. 3b).

Further performance improvement was obtained with the blue-green ratio model (Fig. 3c), as indicated by slopes closer to unity (range:

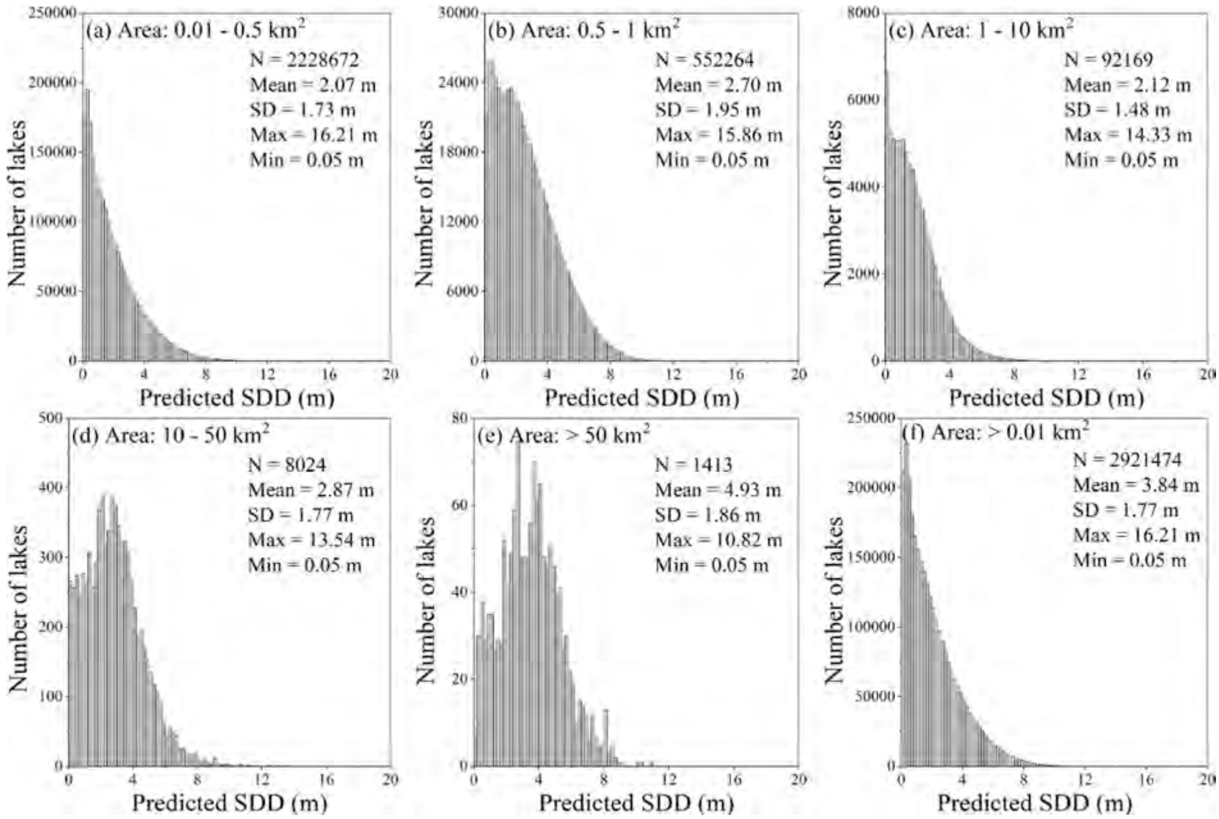

Fig. 8. Histogram of distribution of SDD (Secchi disk depth) for lakes and reservoirs of different sizes across North America. Data are presented by water surface area: (a) <0.1 km^2, (b) between 0.1 and 1 km^2, (c) between 1 and 2 km^2, (d) between 2 and 5 km^2, (e) between 5 and 10 km^2, and (f) >10 km^2.

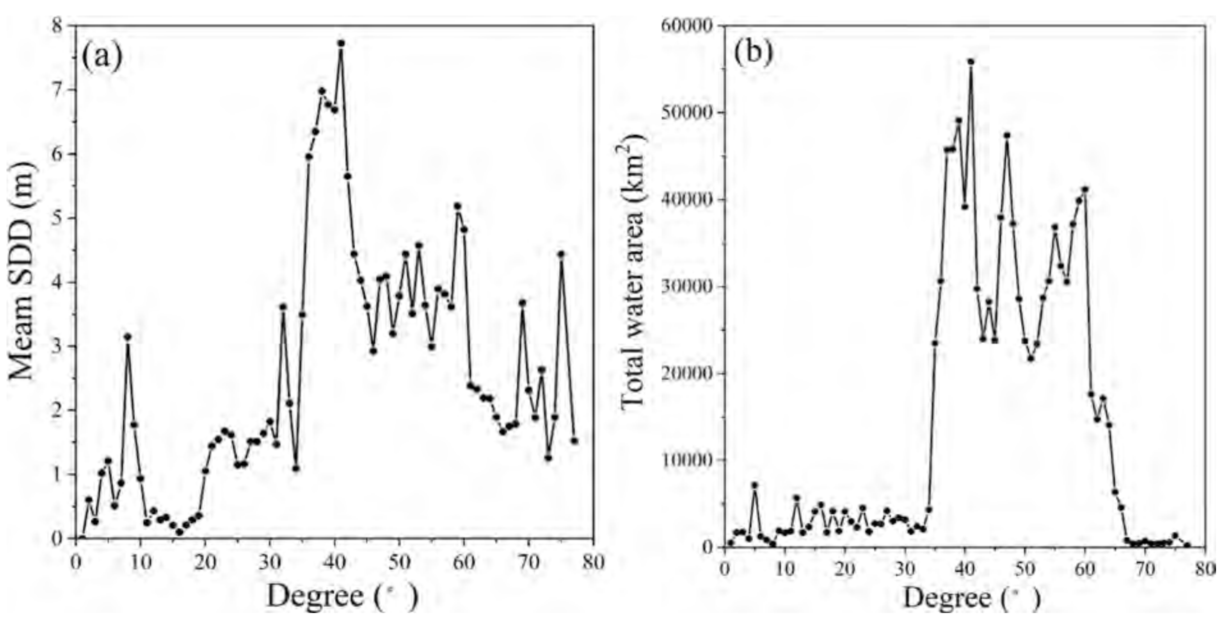

Fig. 9. Latitudinal variation of (a) mean SDD and (b) total lake water surface area across Central America and North America.

0.78–0.91 m with different Landsat sensors) and lower intercepts (0.40 to 1.24 m). Among the four regression models, the RGRB model based on the red-blue plus the blue-green band ratios (as described in Song et al., 2022) emerged as the best-performing model (Fig. 3d). Good evidence was found of a significant association between in situ, and Landsat predicted SDD, irrespective of the Landsat sensor (OLI: $R^2 = 0.82$; ETM+: $R^2 = 0.81$; TM: $R^2 = 0.82$, Fig. 3d). In light of this better performance, the following models were proposed for the continental-scale derivation of SDD. As shown in Eqs. (6)–(8) below, the models included a combination of red-blue and blue-green band ratios from different Landsat sensors:

$$LN(SDD)_{OLI} = -0.76{*}R/B + 5.11{*}B/G - 1.37 \quad (R^2 = 0.82; p < 0.001) \tag{6}$$

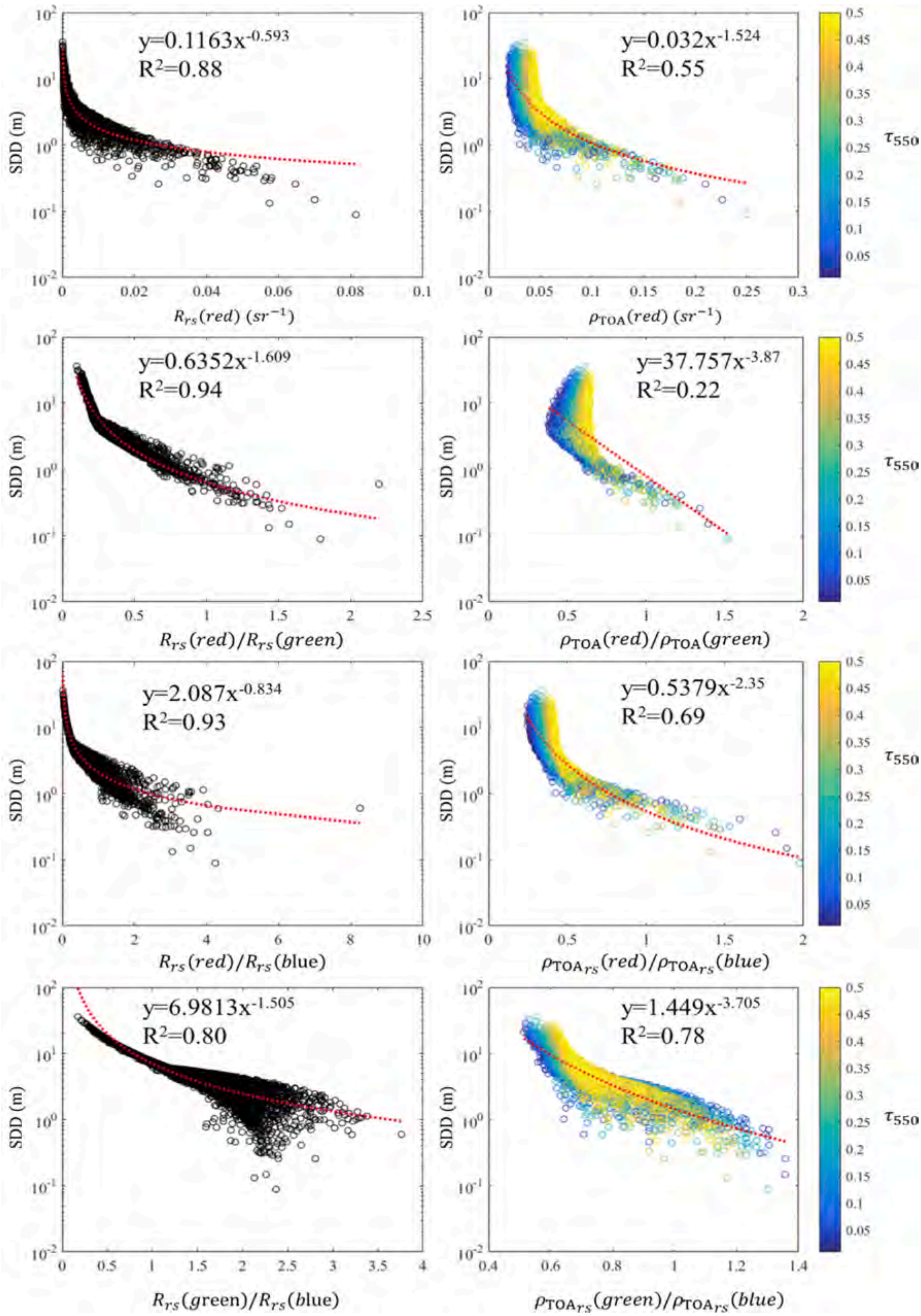

Fig. 10. Correlations between simulated SDD and Landsat OLI indices calculated from simulated $R_{rs}(\lambda)$ (left column) and simulated TOA reflectance (right column), where the ×, a, b, and c represent Landsat OLI red band, the red-green band ratio, the red-blue band ratio, and the green–blue band ratio, respectively, for the simulated CCRR dataset. The red dashed lines represent the regression lines. (For interpretation of the references to colour in this figure legend, the reader is referred to the web version of this article.)

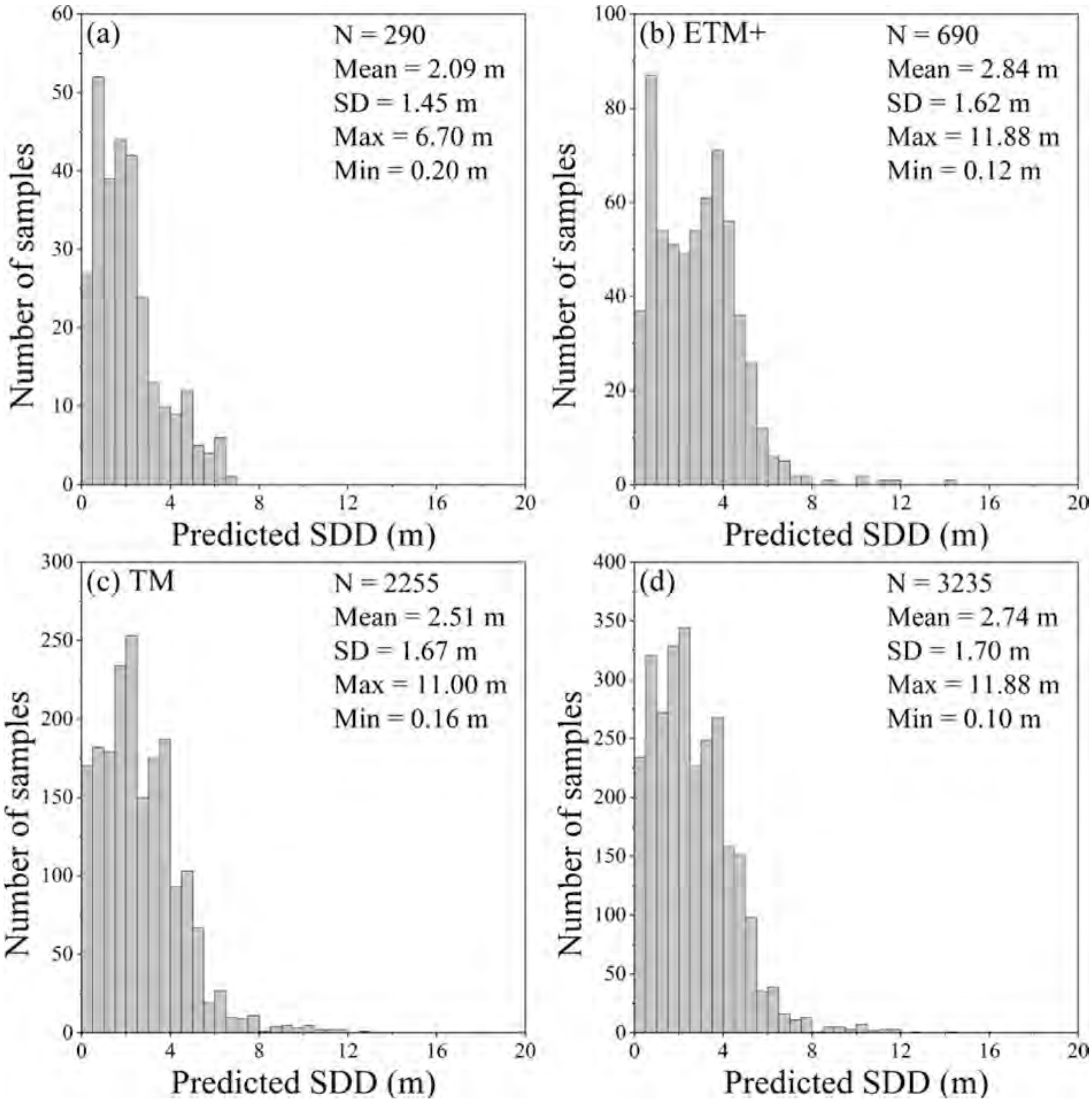

Fig. 11. The frequency distribution of in situ SDD matched up with different Landsat sensors: (a) Landsat OLI, (b) Landsat ETM+, (c) Landsat TM, and (d) the pooled dataset with all Landsat sensors.

$$LN(SDD)_{ETM+} = -2.36R/B + 3.65B/G + 1.48 \quad (R^2 = 0.78; p < 0.001) \tag{7}$$

$$LN(SDD)_{TM} = -2.81{*}R/B + 2.73{*}B/G + 2.96 \quad (R^2 = 0.82; p < 0.001) \tag{8}$$

where B, G, and R are the TOA reflectance for Landsat OLI bands 2, 3, and 4, respectively, and corresponding bands 1, 2, and 3 for Landsat ETM+ and TM, respectively. As shown in Fig. 3d, for all three Landsat sensors, slopes were close to unity (range: 0.86–0.91 m), and values of the intercepts were low (range: 0.38–0.78 m). A transformation of SDD data (LN(SDD)) was adopted to improve goodness-of-fit. The model was selected based on maximum R^2 and minimum values for RMSE, MAPE, and Bias.

There are only a few matchups for Landsat 8 (179 samples in the calibration dataset and 111 in the validation dataset). The SDD range of the Landsat OLI calibration dataset was only from 0.1 to 4.5 m. For empirical models, a wide SDD range of the calibration dataset will ensure the models are more robust in retrieving SDD on a continental scale. Thus, the performance of a unified expression of different models across different Landsat sensors was evaluated using the pooled dataset (Table 3). Using the pooled dataset, the red band model exhibited a low performance ($R^2 = 0.62$; Fig. S2). However, with the pooled data, improved model performance with both the red-blue band ratio ($R^2 = 0.67$) and the blue-green band ratio models ($R^2 = 0.76$). With the pooled data, the best-performing model developed with the Landsat sensor included a combination of the red-blue and blue-green band ratios ($R^2 = 0.81$, $p < 0.001$; Table 3):

$$LN(SDD) = -2.74 \times R/B + 3.01 \times B/G + 2.51 \tag{9}$$

where R, G, and B are TOA reflectance values for red, green, and blue bands of the Landsat OLI/ETM+/TM, respectively. That model (combinations of blue-green and red-blue band ratios) was used as a universal model (Eq. (9)) tuned with the pooled dataset to map SDD for all lakes and reservoirs with surface area ≥ 1 ha across NA.

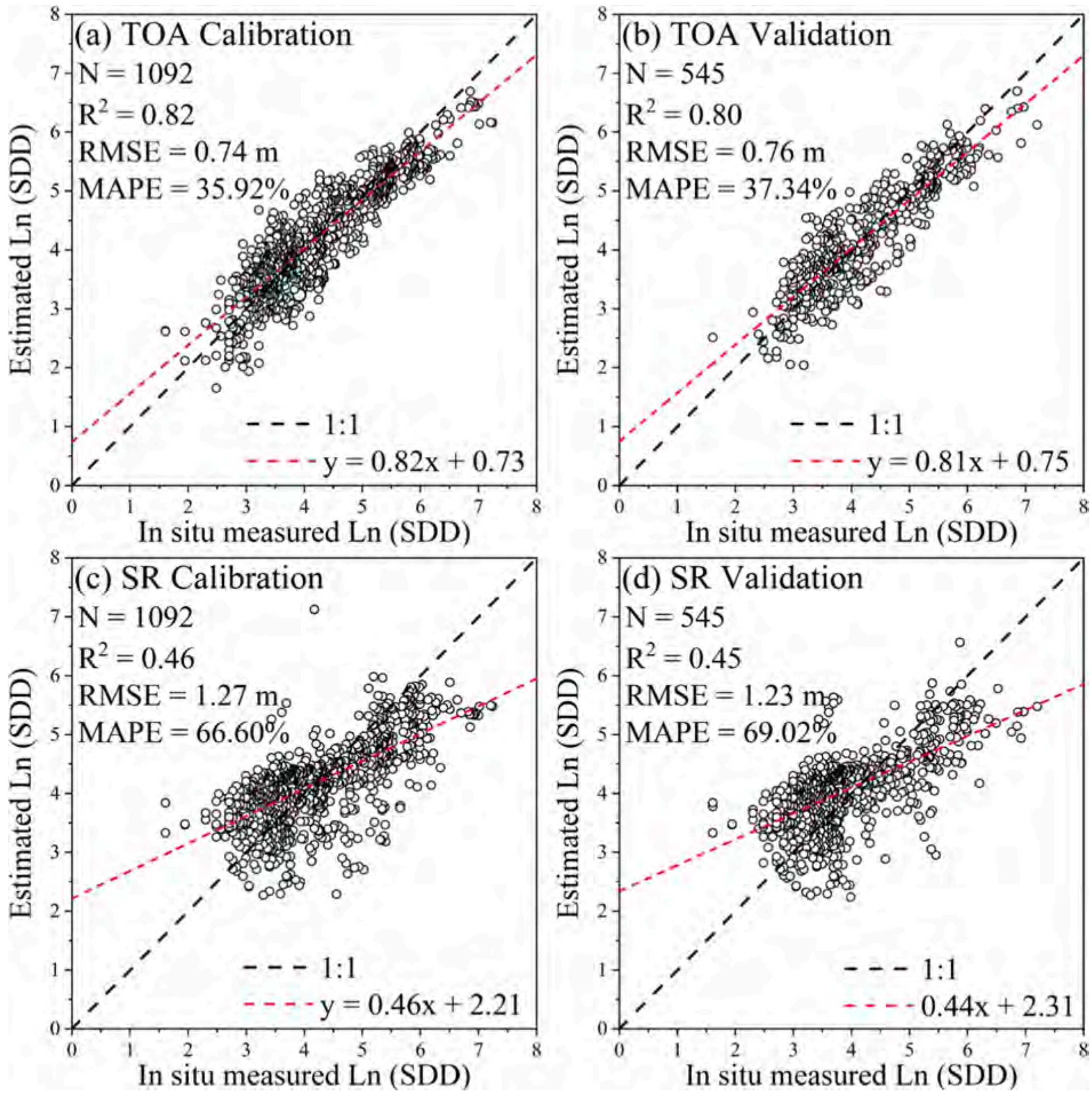

Fig. 12. The calibration and validation of the RGRB model using TOA and SR products, respectively.

3.2. Model validation

Without adjusting the spectral band ratios and model parameters, the proposed RGRB model generally performed well in generating SDD estimates (Fig. 4d, Table 4). As expected, the red band model exhibited larger RMSE, MAPE, and Bias and revealed a major departure of the regression slopes from unity and variations in the slopes and intercepts of the regression lines among the different Landsat sensors (Fig. 4a, Table 4). Likewise, the red-blue band ratio model also exhibited relatively large RMSE, MAPE, and Bias (Fig. 4b, Table 4). The blue-green band ratio model exhibited better performance in terms of lower RMSE and MAPE. These observations were further supported by the slopes between in situ SDD and Landsat predicted values approaching unity (Fig. 4c, Table 4). In terms of the RGRB model, the RMSEs of the models established with Landsat OLI, Landsat ETM+, and Landsat TM of the validation dataset were 1.47 m, 1.05 m, and 0.31 m, respectively; while the MAPEs were 42.4 %, 30.2 % and 25.4 % with the correspondingly Landsat sensor, respectively (Fig. 4d, Table 4). The in situ SDD measurements and the SDD values estimated using the proposed model showed very good agreement ($R^2 = 0.78$), with a slope close to unity and small intercept values with pooled validation dataset (Table 5). The comparison of four regression models showed good model performance when applied to the pooled dataset (Fig. S3). Further, it can be seen that the RGRB model outperformed all the other three modeling approaches, as indicated by lower RMSE, MAPE, and Bias (Table 5). The red-blue model (Fig. S3b) and blue-green model (Fig. S3c) also exhibited stable and acceptable performances.

3.3. Spatial variation of SDD in 2019

In addition to the spatial distribution of lakes and reservoirs throughout NA, large variations in SDD were also observed across the continent (Fig. S4). To graphically display variations in water clarity at the continental scale, we calculated the average SDD for each lake and reservoir. We presented each lake and reservoir as a dot on a map (Fig. 5). The mean SDD of lakes and reservoirs across the continent was 3.84 ± 1.77 m, with large regional variations. In general, lakes and reservoirs with higher SDD generally exhibit larger internal variability

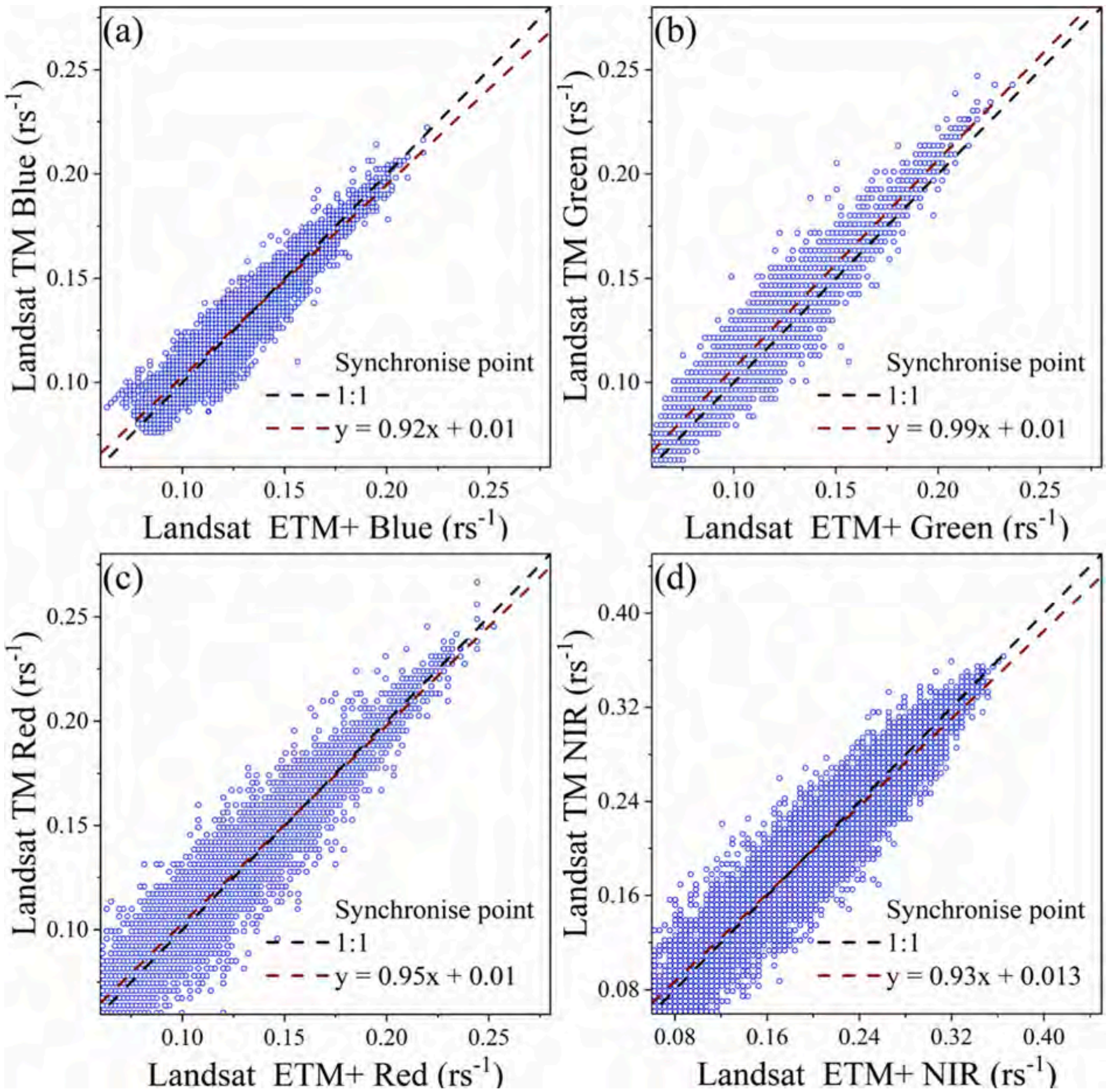

Fig. 13. Relationships between Landsat TM blue (a), green (b), red (c), and NIR (d) bands versus the corresponding spectral bands from Landsat ETM +. The Landsat TM and ETM+ images were acquired on August 1, 2017. (For interpretation of the references to colour in this figure legend, the reader is referred to the web version of this article.)

in SDD (Fig. 5b) and vice versa (Fig. 5a, 5b). For example, for lakes and reservoirs such as Great Salt Lake, Great Slave Lake, Lago de Chapala, and Lake Winnipeg, relatively high SDD was found in the central portion of the lakes and reservoirs, while the shoreline regions exhibited low water clarity (Fig. S7). In contrast, for lakes and reservoirs such as Great Bear Lake, Lake Athabasca, and Salton Lake, only small areas along the shorelines had low water clarity (Fig. S5).

Concerning the areal average of SDD, lake and reservoir water clarity tended to be higher in the United States (5.24 ± 1.44 m) and Canada (3.52 ± 1.80 m) and lower in Greenland (1.98 ± 1.11 m) and Central America (0.84 ± 0.57 m) (Fig. 6). Water clarity was generally higher in high latitude regions where large lakes and reservoirs tend to dominate (see Fig. S7 for the Great Laurentian Lakes and Great Bear Lake).

Significant differences were found in different countries average lake and reservoir clarity and density (Fig. 7). Mean lake and reservoir SDD in Canada was 2.21 ± 1.80 m (N = 2,359,741), which was significantly higher than that in the United States, with an average of 1.05 ± 1.11 m (N = 365,813). Central America SDD was only 0.39 ± 0.57 m (N = 22176). On the contrary, lakes and reservoirs in Greenland showed relatively higher SDD (1.76 ± 1.11 m).

To further examine variations in SDD, we conducted a stratified statistical analysis based on water size. A significant difference in SDD was found among groups of lakes and reservoirs of various sizes. For lakes and reservoirs with areas < 0.5 km^2, 0.5–1 km^2, 1–10 km^2, 10–50 km^2 and >50 km^2, mean SDD were 2.07 ± 1.73 m (N = 2,228,672), 2.70 ± 1.95 m (N = 552,264), 2.12 ± 1.48 m (N = 92,169), 2.87 ± 1.77 m (N = 8,024) and 4.93 ± 1.86 m (N = 1,413), respectively (Fig. 8). Thus, lakes and reservoirs with large water surface areas tend to display higher water clarity, while the smaller lakes and reservoirs tend to be more turbid (Fig. S8). Consequently, a close association was found between log-transformed SDD and water surface area (Fig. S9).

The latitudinal variation of SDD in NA was also examined (Fig. 9). In general, lake and reservoir surface area and water clarity were highest between 35° N and 60° N latitude. In contrast to the high latitude areas where transparent lakes and reservoirs predominate, relatively high turbidity lakes and reservoirs are abundant in the lower latitude regions

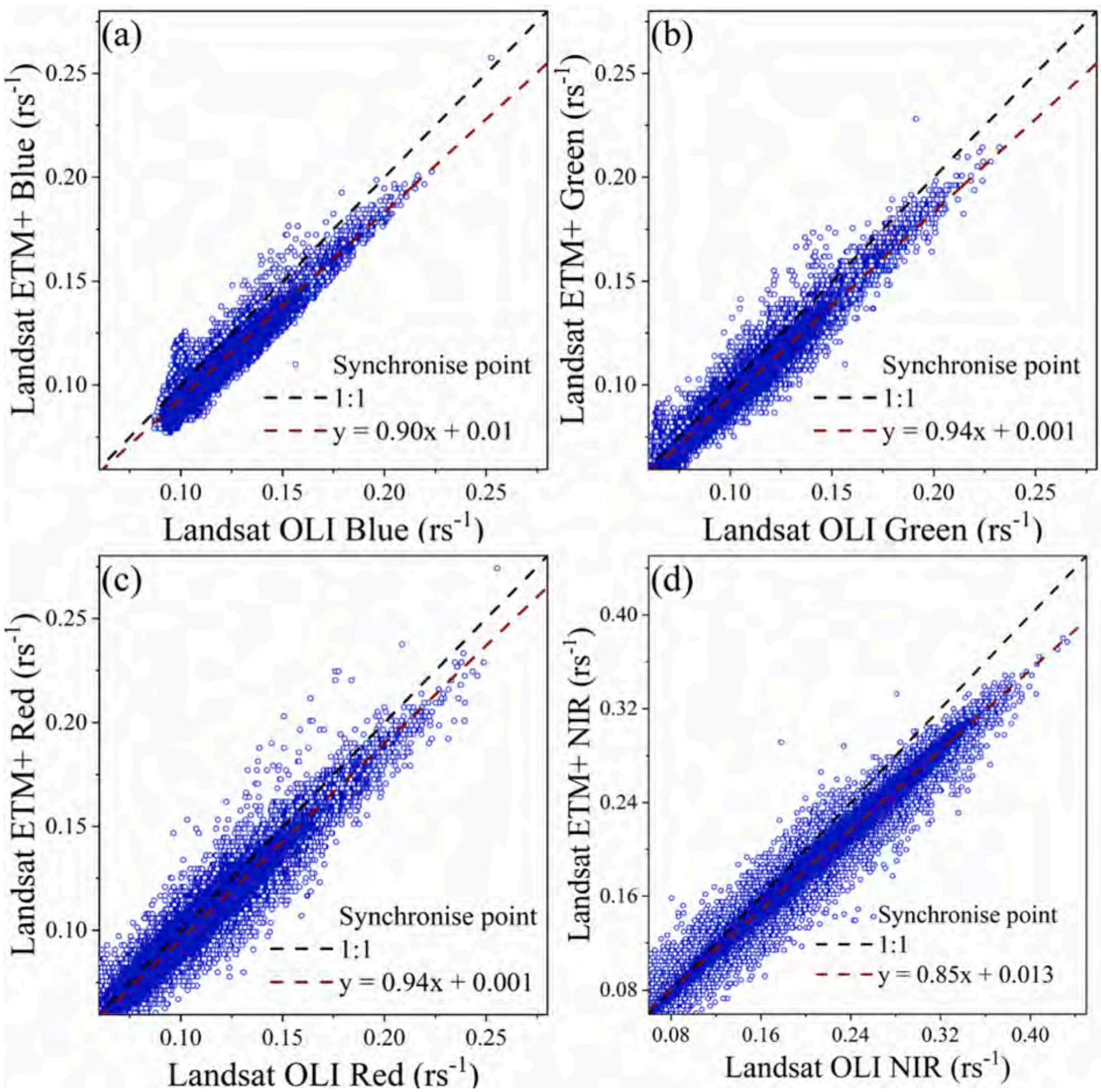

Fig. 14. Relationships between Landsat OLI blue (a), green (b), red (c), and NIR (d) bands versus the corresponding spectral bands from Landsat ETM +. The Landsat TM and ETM+ images were acquired on August 13, 2017. (For interpretation of the references to colour in this figure legend, the reader is referred to the web version of this article.)

where flat landscapes and intensive agriculture occur (Fig. 9).

4. Discussion

4.1. Performances of different spectral indices

As shown by the validation dataset, the RGRB model exhibited reasonable accurate SDD predictions with Landsat imagery data acquired by different sensors. The reason why the blue-green band ratio explained a high percentage of variance in SDD was further explored. We used the simulated dataset (5000 samples) to evaluate the uncertainties in SDD estimate by different spectral indices (e.g., red band, red-green ratio, red-blue ratio, and blue-green ratio). The correlation between the spectral indices calculated from simulated $R_{rs}(\lambda)$ and simulated SDD was first validated. As shown in Fig. 10, the red-green ratio obtained the highest coefficient of determination ($R^2 = 0.94$), followed closely by the red-blue ratio ($R^2 = 0.93$) and single red band ($R^2 = 0.88$). The blue-green ratio showed relatively low performance with $R^2 = 0.80$. Then the simulated $\rho_a(\lambda)$, $\rho_r(\lambda)$, $t_u(\lambda)$, and $t_d(\lambda)$ with specific $\tau_a(\lambda)$ loadings were randomly added to the simulated $R_{rs}(\lambda)$ to obtain the simulated $\rho_{TOA}(\lambda)$. Compared with using the simulated $R_{rs}(\lambda)$, the correlation of each index calculated from simulated $\rho_{TOA}(\lambda)$ and the simulated SDD all decreased markedly, especially for the red-green ratio ($R^2 = 0.22$) and single red band ($R^2 = 0.55$). The two spectral indices used in our model with higher R^2 (red-green ratio: 0.69 and blue-green ratio: 0.78) implied that our algorithm might be more robust for the continental or even global inland water SDD mapping when using Landsat $\rho_{TOA}(\lambda)$ reflectance compared with commonly used single red or blue-green ratio algorithms.

4.2. Model performance evaluations

Our assessment of the performances of the RGRB model has shown that OLI, ETM+ and TM imagery data can be used to monitor SDD variations in lakes and reservoirs, as evidenced by the strength of the relationship between Landsat spectral variables and in situ SDD

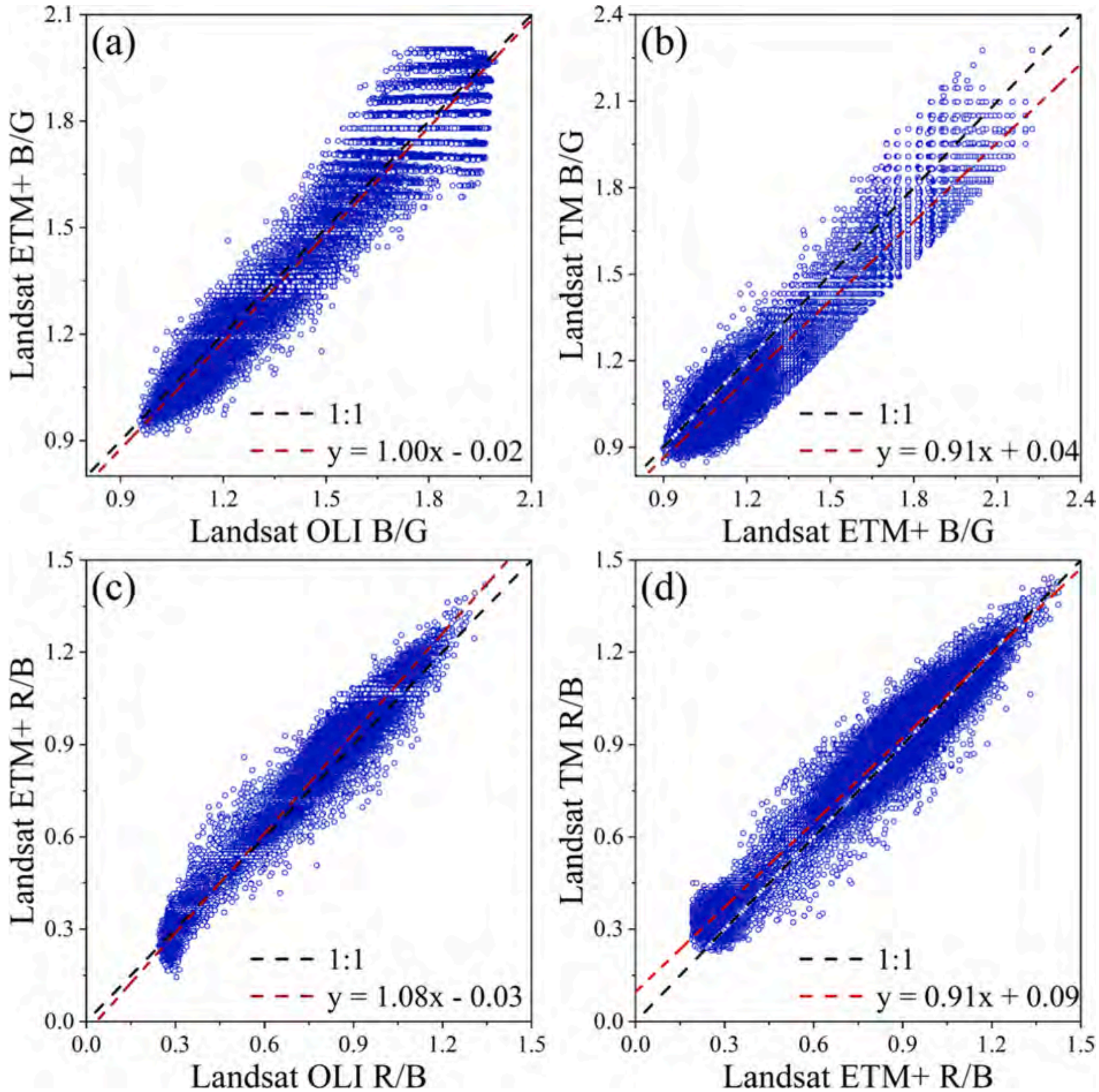

Fig. 15. Relationships between the blue-green band ratios obtained from different sensors: (a) OLI versus ETM+, (b) ETM+ versus TM. Relationships between the red-blue band ratios with different sensors: (c) OLI versus ETM+, (d) ETM+ versus TM. Landsat ETM+ ETM+ and Landsat OLI spectral data reported in panels (a) and (b) were acquired on August 13, 2017. Landsat ETM+ and Landsat OLI spectral data reported in panels (c) and (d) were obtained on August 1, 2017. (For interpretation of the references to colour in this figure legend, the reader is referred to the web version of this article.)

(correlation coefficient: r = 0.91, 0.88 and 0.86, respectively). Landsat OLI had 290 matching sampling points, while Landsat ETM+ and TM had 690 and 2255 points, respectively (Fig. 11). The ranges of the matched SDD values are also significantly different among different groups, with OLI 0.20–6.70 m, ETM+ 0.12–1.188 m, and TM 0.16–1.10 m. As shown in Fig. 11a, the SDD value range matching up with OLI was relatively small, with a low mean (Mean ± SD: 2.09 ± 1.45 m), while ETM+ (Fig. 11b) and TM (Fig. 11c) modeling samples are comparable. The different SDD ranges matching up with images acquired by different Landsat sensors may explain why the coefficients of the regression models varied significantly with red band, red-blue, and red-green models (Fig. 3).

The SDD retrieval model established with OLI and ETM+ data is likely applicable to inland water bodies throughout NA. Different Landsat sensors have been operating during specific periods; the Landsat ETM+ scan line corrector (SLC) has malfunctioned since May 31, 2003, and Landsat TM has stopped collecting data since November 18, 2011, leaving Landsat OLI and Landsat 9 the only Landsat sensors currently operational. Therefore, relationships between sensors need to be established and evaluated in long-term studies using data from all three sensors (Landsat OLI, ETM+ and TM) to assess trends in continental/regional water clarity. Landsat OLI and ETM+ have similar wavelength ranges in the blue, green, red, and NIR bands, and Landsat TM and ETM+ have the same wavelength ranges in the blue, green, red, and NIR bands (Table 2). Because of these spectral overlaps, we tested the consistency of Landsat OLI and ETM+ imagery data collected on the same date and over the same region as Landsat TM and ETM+ images, respectively (Table S1). Results showed high consistency for each Landsat OLI, ETM+, and TM band. Excellent agreement was found between Landsat TM and ETM+ in the blue ($R^2 = 0.91$), green ($R^2 = 0.99$), red ($R^2 = 0.95$), and NIR bands ($R^2 = 0.93$) (Fig. 13). The slopes of the relationships were all >0.92, further indicating the spectral band consistency between TM and ETM+ imagery. Agreement between the OLI and ETM+ sensors was also very good in the green ($R^2 = 0.95$) and NIR

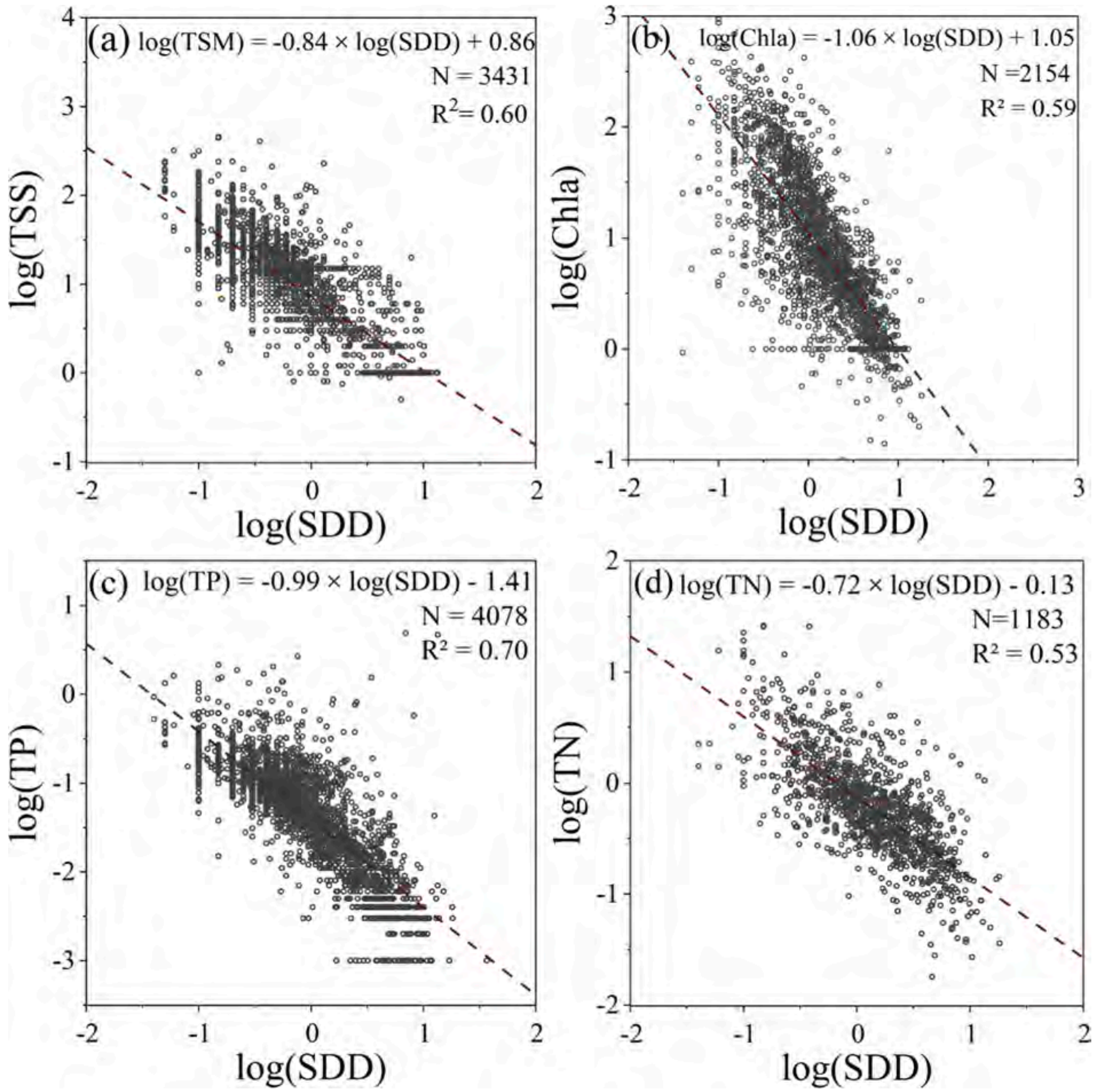

Fig. 16. Relationships between: (a) SDD and TSM, (b) SDD and Chl-a, (c) SDD and TP, and (d) SDD versus TN in the datasets used. Relationships are shown for log-transformed data.

($R^2 = 0.95$) bands, but the consistency was less than ideal in the blue ($R^2 = 0.86$) and NIR band ($R^2 = 0.86$) (Fig. 14). In this instance, the slopes of the relationships varied between 0.85 and 0.94, indicating spectral configuration difference between OLI and ETM+, particularly for the blue and NIR spectral bands (Fig. 14d). Fig. 15(a) and 15(c) were scatter plots of Landsat OLI and Landsat ETM+ TOA reflectance in Blue/Green and Red/Blue band ratios. The comparison results show that the Blue/Green band ratio has a higher $R^2 = 0.98$ while the Red/Blue band ratio has a lower $R^2 = 0.97$. Fig. 15(b) and 15(d) were scatter plots of Landsat ETM+ and Landsat TM TOA reflectance in Blue/Green and Red/Blue band ratios. The linear regression parameters have the higher $R^2 = 0.91$ in Red/Blue band ratios and the lower $R^2 = 0.85$ in Blue/Green band ratios. And the red/blue band ratios are more consistent than the blue/green band ratios. Despite these spectral configuration differences, the proposed RGRB model exhibited stable performance with both calibration and validation datasets (Figs. 3 and 4). Nevertheless, these differences should be considered and proper adjustments made when constructing models that use data collected with multiple Landsat sensors (Fig. 15). Because of the short running time, it is hard to obtain enough matchups to construct SDD models for Landsat 9. The reliable performance of RGRB across different Landsat sensors implied that it could be applied to this sensor to map water clarity in North American lakes and reservoirs with the Landsat OLI data together.

The uncertainties of different time windows set to the RGRB model were also analyzed. When the time window between in situ samplings and satellite overpass was ±3 days, there were 351 matchups (Fig. S10). The RGRB had higher R^2 and lower RMSD and MAPE for the shorter time window. All the evaluation indexes showed a slight improvement compared with the matchups obtained with ±7 days' time window.

GEE has two Landsat reflectance products (TOA and SR products). For all the 3235 samples, we selected 1637 samples to compare the different performances of RGRB when using TOA and SR reflectance products, respectively. Among these 1637 samples, 1092 were used as a calibrated dataset to re-parametrize the RGRB model, as shown in Fig. 12 a.b and Eqs. (10)–(11). The reset 545 samples were used to validate. Compared with the SR product (Fig. 12 c.d), the R^2 increased from 0.45 to 0.80, the MAPD decreased from 69.02 % to 37.34 %, and the RMSE decreased from 1.23 m to 0.76 m. The SR product seems better than the TOA because it is entirely atmospheric corrected. The opposite result implied that the SR products by the land target atmospheric correction methods might not be suitable for the water quality retrieving in North America. Without considering the effect of relative humidity on aerosols, the failure of the ground spectral assumption, or the spatial differences in aerosols of land target atmospheric correction methods when applied to the lakes and reservoirs, these may be the reasons (Liu et al., 2015, Song et al., 2020).

$$\mathrm{TOA} : \mathrm{LN(SDD)} = 1.068^{*}\mathrm{B/G} - 4.253^{*}\mathrm{R/B} + 5.521 \tag{10}$$

$$\mathrm{SR} : \mathrm{LN(SDD)} = -0.417^{*}\mathrm{B/G} - 1.526^{*}\mathrm{R/B} + 6.16 \tag{11}$$

4.3. Model implications

This study is perhaps the first attempt to establish a universal model for mapping SDD of lakes and reservoirs across the NA continent using Landsat imagery. It is a worthwhile effort considering that nearly 43.5 % of the global lakes and reservoirs are in NA (Pekel et al., 2016). The RGRB model using both blue-green and red-blue band ratios showed superior performance compared to most of the previous modeling approaches reported in the literature (Kloiber et al., 2002; McCullough et al., 2012; Song et al., 2020, and Table 1). First, the model exhibited very stable performance with both model calibration and model validation datasets (Fig. 10). Second, this modeling approach can accommodate differences in spectral configuration among the Landsat sensors (TM, ETM+, and OLI). Thus, it has the potential to map water clarity dynamics using archived imagery acquired by Landsat series sensors, which span nearly-four decades (1984–2021). Third, in situ SDDs were collected from lakes and reservoirs encompassing a wide range of optical properties and trophic status (from oligotrophic to hypereutrophic) (Olmanson et al., 2008; Brezonik et al., 2015). Thus, because of the approach adopted for its construction and parameterization, the model should be robust enough and transferable to lakes and reservoirs spanning various optical properties worldwide.

Lake and reservoir water clarity is strongly linked with Chl-a, TSM, TN, and TP (Carlson, 1977; Song et al., 2012, 2014). According to previous studies, water clarity has been used as an effective proxy for evaluating water trophic status (Olmanson et al., 2008; Song et al., 2012, 2014). We collected TSM, Chl-a, TP, and TN. Close relationships between SDD and these four water quality parameters were confirmed (Fig. 16). Therefore, we could use the Landsat-derived SDD through the universal model to generate a trophic state index and evaluate lake and reservoir trophic state for the whole continent of NA through the strong linkage between SDD and these crucial water quality parameters (Fig. 16). According to UN SDGs 2030′s ambient water quality, only 36 % of the world's countries can provide the necessary measured water quality parameters, e.g., Chl-a, Dissolved Oxygen, pH, EC, TN (SDG 6.3.2, 2018). Water clarity is related to these five parameters. Thus, we could use Landsat-derived SDD to meet SDG 6.3.2 by monitoring water quality at large scales, particularly in countries without established water quality monitoring networks, resources, and abilities. Recently, Shen et al. (2020) have developed a framework to link water clarity to SDG 6.3.2 for evaluating water quality using remotely sensed SDD for lakes in east China. A modification of the framework can be used to assess ambient water quality on a national, continental, or even global scale. This approach could be particularly useful for developing countries where research facilities or well-trained technicians are rare. Thus, it could greatly facilitate water quality evaluation and meet the SDG 6.3.2 evaluation requirement (SDG, 2018).

5. Conclusions

We demonstrated that Landsat TOA reflectance data provided by GEE could be used to generate reasonably robust estimates of SDD variation for a large portion of the lakes and reservoirs (≥1 ha in the area; 43 % of all global lakes and reservoirs) in North America. More than 3200 SDD measurements were matched with Landsat spectral data collected within ±7 days of field measurements. The results indicate that the RGRB model based on the blue-green ratio plus the red-blue ratio from Landsat images performed better than other empirical models based on single bands or single band ratios. Using the RGRB model, more than 2.9 million lakes and reservoirs (with surface area ≥ 1 ha) were mapped across NA. A continental-scale assessment of SDD was carried out using this model and Landsat imagery collected during the ice-free season in 2019. Results showed an average SDD of 3.84 ± 1.77 m and some intriguing spatial variations and patterns. Lake and reservoir water clarity in NA decreased from high to low latitude regions. Additionally, the RGRB model exhibited very stable performance and has great potential for application in future investigations of spatial variations and trends in global inland water clarity.

Declaration of Competing Interest

The authors declare that they have no known competing financial interests or personal relationships that could have appeared to influence the work reported in this paper.

Acknowledgments

The research was jointly supported by the National Key Research and Development Program of China (2021YFB3901101), the National Natural Science Foundation of China (No. 42171385) and Youth Innovation Promotion Association of Chinese Academy of Sciences, China (2022228). The authors also thank Dr. Ying Zhao, Tiantian Shao, Jianhang Ma, Jingping Xu, Ming Wang for their assistance with data collection and processing. The authors are grateful for access to Landsat imagery data provided by the USGS through the Google Earth Engine cloud computation platform. The authors also would like to thank the research and regulatory organizations that provided free access to their datasets; without these in situ SDD data, this work would not have been possible.

Appendix A. Supplementary material

Supplementary data to this article can be found online at https://doi.org/10.1016/j.isprsjprs.2022.09.014.

References

Alcamo, J., Florke, M., Marker, M., 2007. Future long-term changes in global water resources driven by socio-economic and climatic changes. Hydrol. Sci. J. 52 (2), 247–275.
Alföldi, T.T., Munday Jr., J.C., 1978. Water Quality Analysis by Digital Chromaticity Mapping of Landsat Data. Can. J. Remote Sens. 4 (2), 108–126.
Allee, R.J., Johnson, J.E., 1999. Use of satellite imagery to estimate surface chlorophyll a and secchi disc depth of bull shoals reservoir, Arkansas, USA. Int. J. Remote Sens. 20 (6), 1057–1072.
Balian, E.V., Segers, H., Martens, K., 2007. The Freshwater Animal Diversity Assessment: an overview of the results.
Bergström, A., Karlsson, J., 2019. Light and nutrient control phytoplankton biomass responses to global change in northern lakes. Glob. Change Biol.
Binding, C.E., Greenberg, T.A., Watson, S.B., Rastin, S., Gould, J., 2015. Long term water clarity changes in North America's Great Lakes from multi-sensor satellite observations. Limnol. Oceanogr. 60 (6), 1976–1995.
Boland, D.H., 1976. Trophic classification of lakes using Landsat-1 (ERTS-1) Multispectral Scanner data. EPA-600/3-76-037. US Environmental Protection Agency, Corvallis, Oregon, 140 p. +app.
Bonansea, M., Rodriguez, C.M., Pinotti, L., Ferrero, S., 2015. Using multi-temporal Landsat imagery and linear mixed models for assessing water quality parameters in Río Tercero reservoir (Argentina). Remote Sens. Environ. 158, 28–41.
Brauman, K.A., Siebert, S., Foley, J.A., 2013. Improvements in crop water productivity increase water sustainability and food security—a global analysis. Environ. Res. Lett. 8 (2), 024030.

Brezonik, P.L., Olmanson, L.G., Finlay, J.C., Bauer, M.E., 2015. Factors affecting the measurement of CDOM by remote sensing of optically complex inland waters. Remote Sens. Environ. 157, 199–215.

Carlson, R.E., 1977. A trophic state index for lakes. Limnol. Oceanogr. 22 (2), 361–369.

Chander, G., Markham, B., Helder, D., 2009. Summary of current radiometric calibration coefficients for Landsat MSS, TM, ETM+, and EO-1 ALI sensors. Remote Sens. Environ. 113, 893–990.

Courville, B.C., Jensen, J.L.R., Dixon, R.W., Fonstad, M.A., 2014. A Landsat-based evaluation of lake water clarity in Maine lakes. Phys. Geogr. 35 (4), 355–368.

Duan, H., Zhang, Y., Zhang, B., Song, K., Wang, Z., Liu, D., Li, F., 2008. Estimation of chlorophyll-a concentration and trophic states for inland lakes in Northeast China from Landsat TM data and field spectral measurements. Int. J. Remote Sens. 29 (3), 767–786.

Feng, L., Hou, X., Zheng, Y., 2019. Monitoring and understanding the water transparency changes of fifty large lakes on the Yangtze Plain based on long-term MODIS observations. Remote Sens. Environ. 221, 675–686.

Feyisa, G.L., Meilby, H., Fensholt, R., Proud, S.R., 2014. Automated water extraction index: A new technique for surface water mapping using Landsat imagery. Remote Sens. Environ. 140, 23–35.

Gorelick, N., Hancher, M., Dixon, M., Ilyhshchenko, S., Thau, D., Moore, R., 2017. Google Earth Engine: Planetary-scale geospatial analysis for everyone. Remote Sens. Environ. 202, 18–27.

Gradilla-Hernández, M.S., de Anda, J., Garcia-Gonzalez, A., Meza-Rodríguez, D., Yebra Montes, C., Perfecto-Avalos, Y., 2019. Multivariate water quality analysis of Lake Cajititlán, Mexico. Environ. Monit. Assess. 192 (1).

Grantham, T.E., Matthews, J.H., Bledsoe, B.P., 2019. Shifting currents: Managing freshwater systems for ecological resilience in a changing climate. Water Security 8, 100049.

Guan, X., Li, J., Booty, W.G., 2011. Monitoring Lake Simcoe Water Clarity Using Landsat-5 TM Images. Water Resour. Manage. 25 (8), 2015–2033.

Hellweger, F.L., Schlosser, P., Lall, U., Weissel, J.K., 2004. Use of satellite imagery for water quality studies in New York Harbor. Estuar. Coast. Shelf Sci. 61 (3), 437–448.

Kloiber, S.M., Brezonik, P.L., Bauer, M.E., 2002. Application of Landsat imagery to regional-scale assessments of lake clarity. Water Res. 36 (17), 4330–4340.

Kotchenova, S.Y., Vermote, E.F.J.A.o., 2007. Validation of a vector version of the 6S radiative transfer code for atmospheric correction of satellite data. Part II. Homogeneous Lambertian and anisotropic surfaces. Appl. Optics. 46, 4455–4464.

Kotchenova, S.Y., Vermote, E.F., Matarrese, R., Klemm, J.r., Frank, J., 2006. Validation of a vector version of the 6S radiative transfer code for atmospheric correction of satellite data. Part I: Path radiance. Part I: Path Radiance. Appl. Opt. 45 (26), 6726–6774.

Kutser, T., 2004. Quantitative Detection of Chlorophyll in Cyanobacterial Blooms by Satellite Remote Sensing. Limnol. Oceanogr. 49 (6), 2179–2189.

Lathrop, R.G., Lillesand, T.M., 1986. Use of thematic mapper data to assess water quality in green bay and central Lake Michigan. Photogramm. Eng. Remote Sens. 52 (5), 10–15.

Lee, Z., Shang, S., Qi, L., Yan, J., Lin, G., 2016. A semi-analytical scheme to estimate Secchi-disk depth from Landsat-8 measurements. Remote Sens. Environ. 177, 101–106.

Lehner, B., Liermann, C.R., Revenga, C., Vörösmarty, C., Fekete, B., Crouzet, P., Döll, P., Endejan, M., Frenken, K., Magome, J., Nilsson, C., Robertson, J.C., Rödel, R., Sindorf, N., Wisser, D., 2011. High-resolution mapping of the world's reservoirs and dams for sustainable river-flow management. Front. Ecol. Environ. 9 (9), 494–502.

Lillesand, T.M., Johnson, W.L., Deuell, R.L., Lindstrom, O.M., Miesner, D.E., 1983. Use of Landsat data to predict trophic status of Minnesota lakes. Photogramm. Photogramm. Eng. Remote Sens. 49 (2), 219–229.

Liu, D., Du, Y., Yu, S., Luo, J., Duan, H., 2019. Human activities determine quantity and composition of dissolved organic matter in lakes along the Yangtze River. Water Res. 115132.

Liu, G., Li, Y., Lyu, H., Wang, S., Du, C., Huang, C., 2015. An improved land target-based atmospheric correction method for Lake Taihu. IEEE J. Sel. Top. Appl. Earth Obs. Remote Sens. 9 (2), 793–803.

Loveland, T.R., Dwyer, J.L., 2012. Landsat: Building a strong future. Remote Sens. Environ. 122 (1), 22–29.

Ludwig, C., Walli, A., Schleicher, C., Weichselbaum, J., Riffler, M., 2019. A highly automated algorithm for wetland detection using multi-temporal optical satellite data. Remote Sens. Environ. 224, 333–351.

McCullough, I.M., Loftin, C.S., Sader, S.A., 2012. Combining lake and watershed characteristics with Landsat TM data for remote estimation of regional lake clarity. Remote Sens. Environ. 123, 109–115.

Mishra, D.R., Kumar, A., Ramaswamy, L., Boddula, V.K., Das, M.C., Page, B.P., Weber, S. J., 2020. CyanoTRACKER: A cloud-based integrated multi-platform architecture for global observation of cyanobacterial harmful algal blooms. Harmful Algae 96, 101828.

Nechad, B., Ruddick, K., Schroeder, T., Oubelkheir, K., Blondeau-Patissier, D., Cherukuru, N., 2015. Coastcolour round robin data sets: a database to evaluate the performance of algorithms for the retrieval of water quality parameters in coastal waters. Earth Syst. Sci. Data 7 (2).

Nelson, S.A., Soranno, P.A., Cheruvelil, K.S., Batzli, S.A., Skole, D.L., 2002. Regional assessment of lake water clarity using satellite remote sensing. J. Limnol. 62 (1s), 27–32.

Olmanson, L.G., Bauer, M.E., Brezonik, P.L., 2008. A 20-year Landsat water clarity census of Minnesota's 10,000 lakes. Remote Sens. Environ. 112 (11), 4086–4097.

Onderka, M., Pekárová, P., 2008. Retrieval of suspended particulate matter concentrations in the Danube River from Landsat ETM data. Sci. Total Environ. 397 (1–3), 238–243.

Page, B.P., Olmanson, L.G., Mishra, D.R., 2019. A harmonized image processing workflow using Sentinel-2/MSI and Landsat-8/OLI for mapping water clarity in optically variable lake systems. Remote Sens. Environ. 231, 111284.

Pekel, J.F., Cottam, A., Gorelick, N., Belward, A.S., 2016. High-resolution mapping of global surface water and its long-term changes. Nature 540 (7633), 418–422.

Ren, J., Zheng, Z., Li, Y., Lv, G., Wang, Q., Lyu, H., Bi, S., 2018. Remote observation of water clarity patterns in Three Gorges Reservoir and Dongting Lake of China and their probable linkage to the Three Gorges Dam based on Landsat 8 imagery. Sci. Total Environ. 625, 1554–1566.

Rodrigues, T., Alcântara, E., Watanabe, F., Imai, N., 2017. Retrieval of Secchi disk depth from a reservoir using a semi-analytical scheme. Remote Sens. Environ. 198, 213–228.

Sayers, M.J., Grimm, A.G., Shuchman, R.A., Deines, A.M., Mychek-Londer, J., 2015. International journal of remote sensing a new method to generate a high-resolution global distribution map of lake chlorophyll. Int. J. Remote Sens. 36 (7), 1942–1964.

Shen, M., Duan, H.T., Cao, Z.G., Xue, K., Song, X., 2020. Sentinel-3 OLCI observations of water clarity in large lakes in eastern China: Implications for SDG 6.3.2 evaluation. Remote Sens. Environ. 247, 111950.

Song, K.S., Li, L., Li, S., Tedesco, L., Hall, B., Li, L.H., 2012. Hyperspectral Remote Sensing of Total Phosphorus (TP) in Three Central Indiana Water Supply Reservoirs. Water Air Soil Pollut. 223 (4), 1481–1502.

Song, K.S., Li, L., Tedesco, L.P., Li, S., Hall, B.E., Du, J., 2014. Remote quantification of phycocyanin in potable water sources through an adaptive model. ISPRS J. Photogramm. Remote Sens. 95, 68–80.

Song, K.S., Liu, G., Wang, Q., Wen, Z.D., Lyu, L.L., Du, Y.X., Sha, L.W., Fang, C., 2020. Quantification of lake clarity in China using Landsat OLI imagery data. Remote Sens. Environ. 243, 111800.

Song, K.S., Wang, Q., Liu, G., Jacinthe, P.A., Li, S.J., Tao, H., Du, Y.X., Wen, Z.D., Wang, X., Guo, W.W., Wang, Z.M., Shi, K., Du, J., Shang, Y.X., Lyu, L.L., Hou, J.B., Zhang, B.H., Cheng, S., Lyu, Y.F., Fei, L., 2022. A unified model for high resolution mapping of global lake (>1 ha) clarity using Landsat imagery data. Sci. Total Environ. 810, 151188.

Sterner, R.W., Keeler, B., Polasky, S., Poudel, R., Rhude, K., Rogers, M., 2020. Ecosystem services of Earth's largest freshwater lakes. Ecosyst. Serv. 41, 101046.

Tao, H., Song, K.S., Liu, G., Wang, Q., Wen, Z.D., Jacinthe, P.A., Xu, X.F., Du, J., Shang, Y.X., Li, S.J., Wang, Z.M., Lyu, L.L., Hou, J.B., Wang, X., Liu, D., Shi, K., Zhang, B.H., Duan, H.T., 2022. A Landsat-derived annual inland water clarity dataset of China between 1984 and 2018. Earth Syst. Sci. Data 14, 79–94.

Tyler, J.E., 1968. The Secchi Disc. Limnol. Oceanogr. 13 (1), 1–6.

Vanhellemont, Q., Ruddick, K., 2018. Atmospheric correction of metre-scale optical satellite data for inland and coastal water applications. Remote Sens. Environ. 216, 586–597.

Verpoorter, C., Kutser, T., Seekell, D.A., Tranvik, L.J., 2014. A Global Inventory of Lakes Based on High-Resolution Satellite Imagery. Geophys. Res. Lett. 41 (18), 6396–6402.

Wang, M., Gordon, H.R., 2018. Sensor performance requirements for atmospheric correction of satellite ocean color remote sensing. Opt. Express.

Watanabe, F., Alcântara, E., Rodrigues, T., Imai, N., Barbosa, C., Rotta, L., 2015. Estimation of Chlorophyll-a Concentration and the Trophic State of the Barra Bonita Hydroelectric Reservoir Using OLI/Landsat-8 Images. Int. J. Environ. Res. Publ. Health 12 (9), 10391–10417.

Zhang, Y.F., Liang, J., Zeng, G.M., Tang, W.W., Lu, Y., Luo, Y., Xing, W.L., Tang, N., Ye, S. J., Li, X., Huang, W., 2020. How climate change and eutrophication interact with microplastic pollution and sediment resuspension in shallow lakes: A review. Sci. Total Environ. 705, 135979.

Zheng, Z.B., Li, Y.M., Guo, Y.L., Xu, Y.F., Liu, G., Du, C.G., 2015. Landsat-Based Long-Term Monitoring of Total Suspended Matter Concentration Pattern Change in the Wet Season for Dongting Lake, China. Remote Sens. 7, 13975–13999.